https://doi.org/10.5194/egusphere-2025-4261
Preprint. Discussion started: 20 October 2025

Dynamics of island mass effect - Part II: Phytoplankton physiological responses.

Guillaume Bourdin[1*], Lee Karp-Boss[1,2], Fabien Lombard[3], Gabriel Gorsky[3], and Emmanuel Boss[1]

[1]School of Marine Sciences, University of Maine, Orono, Maine, USA
[2]Climate Change Institute, University of Maine, Orono, Maine, USA
[3]Laboratoire d'Océanographie de Villefranche-sur-Mer, Sorbonne Université, CNRS, Villefranche-Sur-Mer, France

Correspondence: Guillaume Bourdin (guillaume.bourdin@maine.edu)

Abstract. Island mass effect (IME) refers to the phenomenon of elevated chlorophyll *a* ([Chla]) concentrations around islands, often extending hundreds of kilometers into oligotrophic waters. In this study, we explore the physiological responses and changes in phytoplankton community composition within island mass effect (IME) zones, providing insights into the drivers and ecological impacts of this phenomenon. Here, we study IMEs associated with four different island groups over six-month periods to illustrate how satellite-derived physiological parameters could be used to further our mechanistic understanding of IME. We use a combination of satellite-derived physiological indices and in situ bio-optical data collected during the *Tara* Pacific expedition. We examine mechanisms such as nutrient enrichment and ecological succession that underpin the IME. Our results demonstrate that phytoplankton populations within IME zones experience, on average, reduced physiological stress compared to the surrounding open ocean, likely due to an alleviation of iron limitation. Hence, recurring iron enrichment may be a significant factor of IME across the South Pacific Subtropical Ocean. In some cases, we also detected signatures of decreased phytoplankton stress due to macronutrient limitation associated with local upwellings and increased vertical mixing, highlighting the role of physical processes in supplying macronutrients to the photic zone. While iron enrichment seems to originate mostly from terrigenous/reef inputs, macronutrients can be both from terrigenous/reef origin or vertical entrainment of nutrient-rich deep water to the surface ocean. We also show that IME is often associated with changes in pigment ratios, which indicates changes in phytoplankton community composition. These findings underscore the complex interplay between nutrient availability, community composition, and physiological stress in shaping IME, offering new perspectives on this phenomenon and its ecological significance.

1 Introduction

The island mass effect (IME) refers to different processes that result in the enhancement of chlorophyll *a* concentration [Chla] and phytoplankton biomass around islands, relative to their surrounding ocean. This phenomenon can contribute substantially to regional phytoplankton standing stocks and may have significant impacts on biogeochemical processes and food web dy-

https://doi.org/10.5194/egusphere-2025-4261
Preprint. Discussion started: 20 October 2025

namics in oligotrophic oceans (Gove et al., 2016; Messié et al., 2022; Bourdin et al., 2025). De Falco et al. (2022) suggest that sea surface temperature anomalies around large elevated islands are due to upwelling and downwelling processes, while smaller islands exhibit only localized cooling from current-island interactions. These patterns indicate that multiple nutrient-enriching processes can coexist around a single island, varying seasonally with oceanic and atmospheric forcing. Single-archipelago studies have shown that macronutrient and iron enrichment in the euphotic zone in the vicinity of islands can lead to phytoplankton biomass accumulation and IME formation (Messié et al., 2020; Martinez et al., 2020; Caputi et al., 2019; James et al., 2020; Palacios, 2002; Raapoto et al., 2019; Signorini et al., 1999). Additionally, Martinez et al. (2020) found differences in plankton community composition between island-specific IME events within the Marquesas archipelago, and indicated that interactions between bottom-up nutrient enrichments and top-down control of phytoplankton populations by grazers can be important factors driving IME processes.

To date, most basin-scale studies of IME have relied on [Chla] (Gove et al., 2016; Messié et al., 2022; Bourdin et al., 2025) or chlorophyll fluorescence (Dandonneau and Charpy, 1985) to assess phytoplankton biomass, offering valuable insights into the spatial extent and temporal variability of IME, but without explicitly disentangling the underlying contributing factors. Because variations in [Chla] can result from changes in phytoplankton biomass, community composition, and physiological acclimation to nutrients, SST, and light (Geider et al., 1998), the interpretation of [Chla] as a phytoplankton biomass indicator is susceptible to bias if not concurrently evaluated with other independent proxies of phytoplankton biomass. Such metrics could include proxies for particulate organic carbon (POC; Bishop et al., 1999; Gardner et al., 2003, 2006) or phytoplankton carbon (C_{phyto}; Graff et al., 2015; Behrenfeld and Boss, 2006), which are insensitive to photoacclimation and can be retrieved from satellite observations. Furthermore, because phytoplankton intracellular [Chla] synthesis is upregulated when incident light decreases and downregulated when phytoplankton cells are stressed due to nutrient limitation, we can use the ratio of C_{phyto} to [Chla] to estimate physiological responses to light exposure and nutrient enrichment ($\frac{C_{phyto}}{[Chla]}$ or its inverse; Behrenfeld et al., 2015; Halsey and Jones, 2015; Laws and Bannister, 1980). With information about ambient light and the mixing depth, we can estimate the contribution of photoacclimation to $\frac{C_{phyto}}{[Chla]}$ and therefore deduce information about physiological responses to nutrient availability. Moreover, multiple studies have shown that iron limitation has a distinct signature on phytoplankton fluorescence, with cells under iron limitation exhibiting higher chlorophyll fluorescence for a given incident irradiance and light absorption efficiency (Behrenfeld and Kolber, 1999; Behrenfeld et al., 2006; Greene et al., 1994; Kolber et al., 1994; Olson et al., 2000; Behrenfeld and Milligan, 2013). Behrenfeld et al. (2009) used this characteristic to calculate the fluorescence quantum yield (Φ_{Sat}) from remote sensing data and assess phytoplankton iron stress across ocean basins.

Building on these relationships, new insights into phytoplankton physiology can be gained in the context of the IME. Here, we examine spatial and temporal variations in macronutrient and iron stress responses of phytoplankton, comparing between communities in coastal water of islands, communities in water masses under the influence of the IME that have been advected offshore, and communities in the adjacent background oligotrophic ocean. We integrate high-resolution in situ bio-optical proxies with satellite data to assess covariance between nutrient stress responses, increases in biomass, and potential changes in community composition to investigate the type of nutrient enrichments associated with IME, their origin, and their ecological consequences on surface plankton communities.

https://doi.org/10.5194/egusphere-2025-4261
Preprint. Discussion started: 20 October 2025

To capture the spectrum of IME responses across the South Pacific Subtropical Gyre (SPSG), this paper presents observations from four island groups (Rapa Nui, Society Islands, Samoa, and Fiji) with varying size, bathymetry, elevation, latitude, and longitude, and consequently are associated with a wide range of IME spatial and temporal extents and [Chla] enhancement (Bourdin et al., 2025). This approach allows a more mechanistic understanding of the likely processes driving the IME. While this approach is presented here in the context of the IME, it is applicable to other studies of mesoscale processes in the ocean, such as upwelling systems and river discharge.

2 Method

2.1 Case study islands

We selected four study regions distributed along a longitudinal gradient of the subtropical and tropical South Pacific Ocean. These regions were sampled as part of the basin-scale survey conducted during the *Tara* Pacific expedition (2016 - 2018 Gorsky et al., 2019; Lombard et al., 2023). The selected regions span a gradient of oceanographic conditions, ranging from the ultra-oligotrophic Eastern Basin (near Rapa Nui) to the moderately oligotrophic Western Pacific Basin (near Fiji and Tonga). Island densities, size, and geomorphic types vary between and within these regions (Table 1). For instance, the region studied around Rapa Nui in the Eastern Pacific encompasses 2 islands and 3 submerged reefs, while the region studied around Fiji and Tonga in the Western Pacific encompasses 158 islands and 306 submerged reefs.

The spatial and temporal dynamics of IMEs and their associated chlorophyll a enhancement have been characterized for each of these case study regions (Bourdin et al., 2025). Here, we extend this analysis to include physiological indicators derived from bio-optical and remote sensing measurements to gain new insights about the underlying mechanisms that contribute to the observed chlorophyll a enhancement

2.2 In situ data collection

We measured inherent optical properties (IOPs), including absorption (a), attenuation (c), and backscattering (b_b), along the *Tara* Pacific transect, using Seabird's ACs spectrophotometer and ECO-BB3 integrated into a continuous flow-through system. We calculated particulate absorption (a_p), particulate attenuation (c_p), and particulate backscattering (b_{bp}) by correcting a, c, and b_b for instrument drift, bio-fouling, and the influence of dissolved matter, based on hourly measurements of 0.2 μm filtered seawater (Dall'Olmo et al., 2009; Slade et al., 2010; Boss et al., 2019). We derived bio-optical proxies for phytoplankton biomass and community composition from a_p and c_p, benefiting from the high sampling resolution of the continuous sampling system to detect gradients of changes in community composition along the sampling transect. We calculated the line-height of the a_p peak of [Chla] at 676 nm (a_{p676LH}) (Boss et al., 2013) and decomposed all a_p spectra into Gaussian functions aligned with the light absorption peaks of specific accessory pigments (Chase et al., 2013). Each day, around 10:30 am local time, we collected surface water samples for pigment analysis via high-pressure liquid chromatography (HPLC). We estimated [Chla] from a_p by correlating total [Chla] measured via HPLC with the amplitude of a_{p676LH} (Fig. A2). Similarly, we

https://doi.org/10.5194/egusphere-2025-4261
Preprint. Discussion started: 20 October 2025

Table 1. Island and submerged reef characteristics of the studied regions. Island geomorphic types from Nunn et al. (2016).

Region	Total number	30 m isobath area	Island geomorphic types
Rapa Nui	Islands = 2 Reefs = 3	min = 0.6 km^2 mean = 51 km^2 max = 218 km^2 sum = 256 km^2	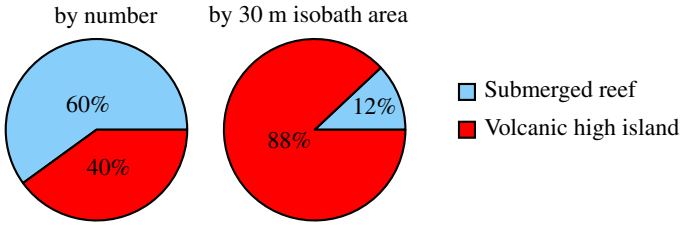
Society Isl.	Islands = 91 Reefs = 17	min = 0.2 km^2 mean = 178 km^2 max = 1,972 km^2 sum = 19,190 km^2	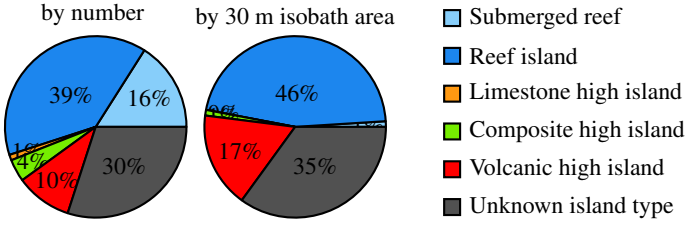
Samoa	Islands = 59 Reefs = 92	min = 0.2 km^2 mean = 104 km^2 max = 2,027 km^2 sum = 15,740 km^2	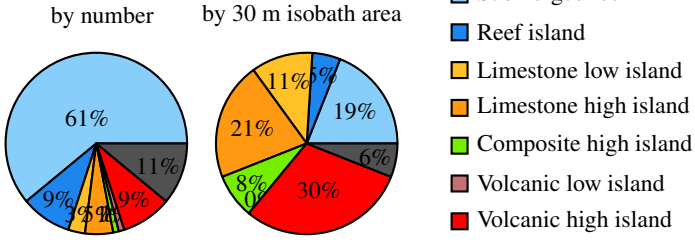
Fiji-Tonga	Islands = 158 Reefs = 306	min = 0.2 km^2 mean = 223 km^2 max = 18,301 km^2 sum = 103,616 km^2	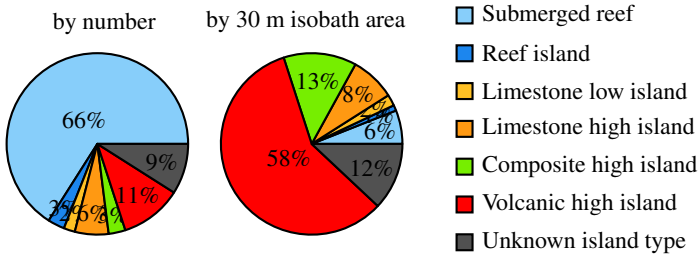

estimated accessory pigment concentrations from continuous underway measurements by relating concurrent pigment concentrations derived from HPLC to the amplitudes of a_p Gaussian functions (Fig. A2). Photo-protective carotenoid concentrations ([PPC]) were estimated from the Gaussian function centered on 492 nm, photosynthetic carotenoid concentrations ([PSC]) were estimated from the Gaussian function centered on 523 nm, chlorophyll *c* concentrations ([Chlc]) were estimated from the Gaussian function centered on 638 nm, and chlorophyll *b* concentrations ([Chlb]) were estimated from the Gaussian function centered on 660 nm (Table 2). We investigated changes in pigment composition along the *Tara* Pacific transect sampled using the ratio of these accessory pigments to [Chla] (e.g. $[PSC]/[Chla]$; Table 2). Phycoerythrin concentrations were not measured as part of the HPLC analysis, thus we estimated the relative concentrations of phycoerythrin using the ratio of the

https://doi.org/10.5194/egusphere-2025-4261
Preprint. Discussion started: 20 October 2025

Gaussian absorption function centered on the phycoerythrin absorption peak (i.e. 550 nm Chase et al., 2013) to the Gaussian absorption function centered on 676 nm, the [Chla] absorption peaks (i.e. $a_{gauss}550/a_{gauss}676$). To quantify changes in the mean size of suspended particles, we computed the slope exponent of c_p (Boss et al., 2001, i.e. γ_{c_p} which is inversely proportional to mean particle size;). Additionally, we measured sea surface temperature (SST) and salinity (SSS) with a Seabird SBE45 thermo-salinograph integrated into the flow-through system. We also continuously recorded above-water instantaneous photosynthetically available radiation (iPAR) from the aft deck of *Tara*, using a cosine PAR sensor (QCP2150; Biospherical Instruments) positioned 5 m above sea level. All variables derived from in situ continuous underway data are described in Tables 2 and 3 and are available at NASA's SeaBASS repository. We collected daily discrete samples of surface seawater to estimate the concentrations of dissolved inorganic nitrogen (i.e., nitrates and nitrites), phosphate, silicate, and total iron (see sampling protocols in Lombard et al., 2023; Gorsky et al., 2019).

Table 2. Description of bio-optical proxies computed from in situ underway data only

Variables	Description
Particulate attenuation at 660 nm (c_p660)	Proxy for particulate organic carbon (Gardner et al., 2006; Behrenfeld and Boss, 2006).
Mean particulate size index (γ_{c_p})	Proxy for mean size of particles mostly sensitive to particles in the size range of 0.2-20 μm. Small values (~ 0) represent assemblies rich in larger particles, while large values (~ 1) represent assemblies rich in smaller particles (Boss et al., 2001).
Normalized chlorophyll *b* ($[Chlb]/[Chla]$)	chlorophyll *b* normalized by total [Chla]. Proxy for green algae relative concentrations (Kramer and Siegel, 2019).
Normalized chlorophyll *c* ($[Chlc]/[Chla]$)	Chlorophyll *c* normalized by total [Chla]. Proxy for diatoms and other red algae relative concentrations (Kramer and Siegel, 2019).
Normalized photosynthetic carotenoids ($[PSC]/[Chla]$)	Photosynthetic carotenoids normalized by total [Chla]. Proxy for diatom relative concentrations (Kramer and Siegel, 2019).
Normalized photo-protective carotenoids ($[PPC]/[Chla]$)	Photo-protective carotenoids normalized by total [Chla]. Proxy for light acclimation of phytoplankton cells (Caferri et al., 2022) and phytoplankton community composition (Kramer and Siegel, 2019).
Normalized phycoerythrin ($a_{gauss}550/a_{gauss}676$)	Phycoerythrin normalized by total [Chla]. Computed as the ratio of Gaussian absorption centered on phycoerythrin absorption peak (550 nm) and Gaussian absorption centered on $[Chla]$ absorption peak (676 nm; Chase et al., 2013). Phycoerythrin pigments are photosynthetic pigments specific to cyanobacteria (e.g. *Synechococcus* spp., *Prochlorococcus* spp., *Trichodesmium* spp., *Richelia* spp., ...). Proxy for relative cyanobacteria concentration.

2.3 Satellite products: phytoplankton biomass indicators

We computed level-2 (L2) satellite products from the Moderate Resolution Imaging Spectroradiometer (MODIS), the Visible Infrared Imaging Radiometer Suite (VIIRS), and the Ocean and Land Colour Imager (OLCI) level-1 data following Bourdin

https://doi.org/10.5194/egusphere-2025-4261
Preprint. Discussion started: 20 October 2025

Table 3. Description of bio-optical and physical variables computed from satellite data.

Variables	Source	Description
Chlorophyll *a* concentration ([Chla])	In situ & satellite	The most commonly used proxy for phytoplankton biomass. Per cell, [Chla] can be modulated due to physiological acclimation to light, nutrient availability, and temperature, and also varies among different phytoplankton species (Geider et al., 1998).
Particulate backscattering (b_{bp})	In situ & satellite	Proxy for biomass that is not modulated by physiological adaptation, but is also sensitive to non-algal particles. b_{bp} represents the backscattering properties of all suspended particulate matter, inorganic and organic. In coastal waters, it can be used to highlight zones with high sediment loads carried into the ocean via runoff. These zones can also have higher terrestrial nutrient enrichment. In the open ocean, far away from riverine inputs, b_{bp} is modulated primarily by phytoplankton and co-varying organic particles.
[Chla] to phytoplankton carbon (C_{phyto}) ratio ($[Chla]/[C_{phyto}]$)	In situ & satellite	Represents the proportion of [Chla] per phytoplankton carbon unit and is modulated by physiological adaptation related to SST, light, and nutrients availability (e.g. lower light = higher $Chla/C_{phyto}$; Geider et al., 1998).
Macronutrient limitation stress (η')	Satellite only	Indicate physiological stress of phytoplankton cells due to macronutrient limitation (moderately stressed for $0.2 > \eta' \geq 0.6$ and very stressed for $\eta' > 0.6$; see Appendix 2.4).
Fluorescence quantum yield (Φ_{Sat})	Satellite only	Indicate physiological stress of phytoplankton cells due to iron (higher Φ_{Sat} = higher stress; Behrenfeld et al., 2009).
Sea surface temperature (SST)	In situ & satellite	Can be used to detect physical processes, e.g. mesoscale features such as upwellings and eddies, and often inversely vary with macronutrient concentration (Goes et al., 1999).

et al. (2025) method; we built two sets of satellite data, a 'calibration dataset' and a 'study dataset'. We downloaded the 'calibration dataset' for the entire area covered by the *Tara* Pacific transect (May 2016 to October 2018 see Gorsky et al., 2019; Lombard et al., 2023). The 'study dataset' consisted of four six-month-long sequences of satellite images in the vicinity of the islands of interest. We applied a polynomial-based atmospheric correction (POLYMER version v4.17beta2; Steinmetz et al., 2011; Steinmetz, last access: 2023-12-22) on both datasets to compute L2 remote sensing reflectance data (R_{rs}) using ancillary data from the European Centre for Medium-Range Weather Forecasts reanalysis model version 5 (i.e. ERA5). We removed poor-quality data pixels by applying the flag recommendations of POLYMER (see reference POLYMER flags, last access: 2024-08) and projected each satellite scene onto an equally spaced 1-km spatial resolution plate-carré reference grid using a nearest-neighbor interpolation from Python's SciPy library. We corrected R_{rs} for Raman scattering (Lee et al., 2013) and derived particulate back-scattering coefficient b_{bp} at 430 nm and 550 nm using the quasi-analytical algorithm V6 (Lee et al., 2002, 2009). We estimated [Chla] using the blended CI-OCx algorithm applying the coefficients derived for each sensor

https://doi.org/10.5194/egusphere-2025-4261
Preprint. Discussion started: 20 October 2025

(Hu et al., 2019; O'Reilly and Werdell, 2019). We estimated phytoplankton carbon (C_{phyto}) using the empirical relationship between $b_{bp}(470nm)$ and C_{phyto} (Graff et al., 2015). Following (Bourdin et al., 2025), we computed surface-area integrated [Chla] as a proxy for surface phytoplankton biomass integrated over entire IME and BO zones, in two-dimensional metric tons of chlorophyll *a* ($t\ m^{-1}$), by summing the [Chla] of each pixel within IME and BO zones multiplied by the area of that pixel:

$$\sum[Chla]_{IME} = \sum_{n=1}^{N_{pixel_{IME}}} [Chla]_n \times area_{pixel_n} \quad (1)$$

All variables derived from satellite data are described in Table 3.

2.4 Satellite products: phytoplankton physiological stress indicators

We computed two biomass-independent phytoplankton nutrient-stress indices. The fluorescence quantum yield (Φ_{Sat}) is indicative of the physiological stress of phytoplankton cells due to iron limitation (higher Φ_{Sat} = more iron stress) and was computed using intermediate products of [Chla], normalized fluorescence line height ($nFLH$), and instantaneous photosynthetically available radiance (iPAR) (Behrenfeld et al., 2009). iPAR was obtained from the output of the function l2gen of SeaDAS (Carder et al., 2003), and the computation of $nFLH$ is detailed in the supplementary section A1.

Huot et al. (2025) raised concerns about the limitations of using MODIS-Aqua data to compute Φ_{Sat} and infer phytoplankton iron stress. MODIS-Aqua overpass time (~13:30 local at the equator) coincides with the time of the day when non-photochemical quenching (NPQ) is maximal, significantly reducing the signal-to-noise ratio of chlorophyll fluorescence after NPQ normalization (that is, $FChla_{NPQ}$) and, consequently, Φ_{Sat}. In the present study, we also computed Φ_{Sat} from MODIS-Terra and OLCI Sentinel-3a, which sample the equator around 10 and 10:30 local time when the NPQ is likely different from the NPQ at the time of MODIS-Aqua overpass. Because the final product Φ_{Sat} is merged from MODIS-Aqua, MODIS-Terra, and OLCI Sentinel-3a, it benefits from an improved signal-to-noise ratio due to the combination of measurements taken at different times of the day. The quality of Φ_{Sat} computed here also benefited from the use of the POLYMER atmospheric correction scheme, which improves data retrieval around clouds and in sun-glint conditions. This is particularly important because the intermediate product of $nFLH$ often shows artificially high values near clouds, likely due to the adjacency effect.

We derived a second physiological proxy that is indicative of phytoplankton stress due to macronutrient limitation. When incident light decreases, phytoplankton cells maintain their growth rate by upregulating chlorophyll pigment synthesis to compensate for the decreased solar energy available (Falkowski and Owens, 1980; Laws and Bannister, 1980). In contrast, phytoplankton cells under macronutrient stress downregulate chlorophyll pigments synthesis (Behrenfeld et al., 2015; Halsey and Jones, 2015; Laws and Bannister, 1980). The ratio of [Chla] to C_{phyto} for a given growth irradiance represents the total physiological stress ($\eta_{obs} = \frac{[Chla]}{[C_{phyto}]}$), and encompasses the physiological stress due to SST, light, and macronutrients availability (Geider et al., 1998; Halsey and Jones, 2015; Laws and Bannister, 1980). Although small changes in $[Chla]/[C_{phyto}]$ have been attributed to temperature variations for a single species in ex situ experiments (Wang et al., 2009), it is likely that the species present in natural assemblages are adapted to their ambient temperature conditions. Given that SST is relatively homogeneous in this region on the timescale of physiological adaptation (i.e. a few days), we assume that all species are adapted to

https://doi.org/10.5194/egusphere-2025-4261
Preprint. Discussion started: 20 October 2025

their ambient temperature conditions, making the impact of SST on $[Chla]/[C_{phyto}]$ negligible at the community level. Consequently, we can isolate the physiological stress due to macronutrient limitation (η') by normalizing η_{obs} by the photoadaptation effect. As part of this process, we computed the median light in the mixed layer (I_{ML}) as follows:

$$I_{ML} = PAR \times e^{-0.5 \times MLD \times Kd_{PAR}} \; [E\, m^{-2}\, d^{-1}] \tag{2}$$

where MLD is the mixed layer depth extracted from the Copernicus Marine Service Global Ocean Physics Reanalysis products (European Union-Copernicus Marine Service, 2019), PAR is the standard daily PAR output of the function l2gen of SeaDAS (Frouin and Pinker, 1995), and Kd_{PAR} is the diffuse attenuation coefficient of photosynthetically available radiance. Kd_{PAR} was approximated from the 1% light horizon (Z_{eu}):

$$Kd_{PAR} = -\frac{ln(0.01)}{Z_{eu}} \; [m^{-1}] \tag{3}$$

where Z_{eu} is estimated from [Chla] following Morel et al. (2007) equation 10:

$$log_{10} Z_{eu} = 1.524 - 0.436X - 0.0145X^2 + 0.0186X^3 \; [m] \tag{4}$$

with $X = log_{10}[Chla]$. We partitioned all I_{ML} and η_{obs} of the four case study regions into two-dimensional bins spanning the entire dynamic range of I_{ML} and η_{obs} of the entire dataset. Because the quantity of level-2 data is too large for our computing capacity, we used 8-day medians merged products of all variables used in this computation (see merging method section 2.5). We identified the 1^{st} and 95^{th} percentiles of η_{obs} for each I_{ML} bin to which we fitted a simple exponential model (Fig. 1):

$$\hat{\eta}_{obs} = A + B \times exp^{-C \times I_{ML}} \tag{5}$$

The model equations fitted on the 1^{st} and 95^{th} percentiles of η_{obs} represent the range of acclimation for the entire dataset.

For each pixel, we computed the difference between the macronutrient replete state ($\hat{\eta}_{obs_{max}}$) and the observed state η_{obs} relative to the full span of η for the pixel's given I_{ML} to provide a quantitative metric of the degree of macronutrient stress:

$$\eta' = \frac{\hat{\eta}_{obs_{max}} - \eta_{obs}}{\hat{\eta}_{obs_{max}} - \hat{\eta}_{obs_{min}}} \; [unitless] \tag{6}$$

Thus, η' is scaled to the parameter space of the specific remote sensing dataset used for this study, and is representative of the relative nutrient stress in the studied regions over the 6-month time series. We arbitrarily defined three macronutrient stress categories, classifying phytoplankton populations as macronutrient-replete when $\eta' \leq 0.2$ (including negative values), moderately stressed when $0.2 < \eta' \leq 0.6$, and highly stressed when $\eta' > 0.6$.

2.5 Satellites products adjustment and merging

Satellite estimates of SST, [Chla], and iPAR (different from the daily PAR used in η' computation) were individually calibrated against in situ measurements obtained from the underway system of the ship to minimize inter-sensor variability and biases. We performed match-ups and robust linear regressions between SST, [Chla], and iPAR measured in situ from the continuous

https://doi.org/10.5194/egusphere-2025-4261
Preprint. Discussion started: 20 October 2025

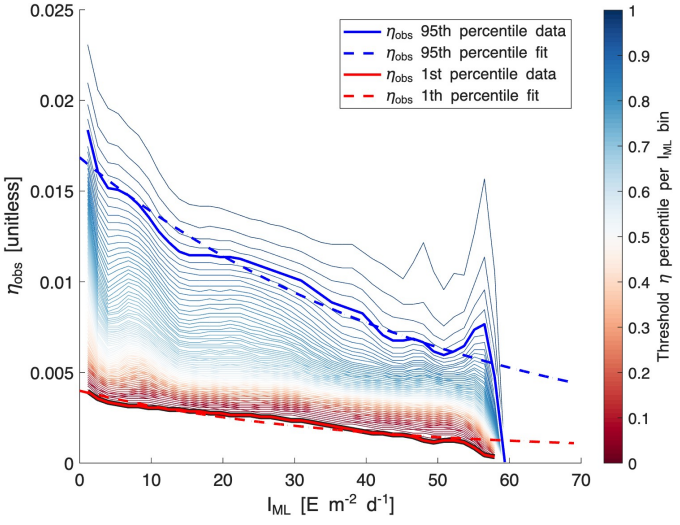

Figure 1. Percentiles of η_{obs} per I_{ML} bins. The blue and red solid lines highlight the 95^{th} and 1^{st} percentiles in each I_{ML} bin. The dashed lines represent the equations Eq. 5 fitted on them.

underway system and their satellite counterparts derived from the calibration dataset (Appendix A2). We used the parameters from their respective robust linear regressions (see Table A1) to produce "calibrated" products before merging them. For parameters derived from remote sensing data with no comparable in situ measurements (e.g. Φ_{Sat}), we adjusted the values from all sensors to align with those of MODIS-Aqua, minimizing inter-sensor discrepancies. This alternative method improved the smoothness of the final merged product and the delineation of spatial patterns. However, potential biases associated with the retrieval of products not calibrated against in situ data remained unconstrained. Although in situ b_{bp} data were available, the relation between in situ b_{bp} and satellite b_{bp} was very sensitive to match-up criteria, and the linear regressions were not well constrained (see Appendix A4). The coefficients used to align the data from different satellite sensors with in situ b_{bp} were inaccurate, leading to noisy merged satellite b_{bp} products. Moreover, an artifact was discovered in MODISA and MODIST b_{bp} maps in ultra-oligotrophic regions ($[Chla] < 0.04\ mg\ m^{-3}$; see Appendices A3 and A4). Therefore, only OLCI and VIIRS-SNPP b_{bp} were binned into the 8-day median products, and OLCI was nudged to best match VIIRS-SNPP's values. We performed this cross-satellite sensor nudging only when: (1) at least 10% of the total pixels of the adjusted sensor and the reference sensor were valid (i.e. unflagged), (2) the slope of the fit was positive, (3) $R^2 >= 0.9$, and (4) $nRMSE <= 10\%$. Before computing the merged products of a given 8-day period and a given region, we grouped all re-projected level-2 images and removed outliers based on the distribution of all individual measurements of the grouped scenes (following the same outlier removal method as in Bourdin et al., 2025, Appendix C). For each case study presented here, we produced a 6-month-long time series of 8-day medians of each of the variables presented in Table 3, following the approach of Bourdin et al. (2025). Each case study region was centered geographically on an island sampled during the *Tara* Pacific expedition, and each 6-month time series was centered temporally on the day of in situ sampling by *Tara* (Gorsky et al., 2019; Lombard et al., 2023). We

https://doi.org/10.5194/egusphere-2025-4261
Preprint. Discussion started: 20 October 2025

propagated the error associated with the satellite product retrieval, nudging, and merging throughout each step to represent the final binned product uncertainty denoted as the standard error of mean (i.e. SEM) of the merged product (e.g. $SEM^{f}_{[\Phi_{Sat}]_{IME}}$; see Appendix A4). We used this final uncertainty to determine if changes associated with an IME are significant.

2.6 Island Mass Effect Detection

We detected IMEs using an iterative method to define a [Chla] contour around each individual IME (see method in Bourdin et al., 2025). We used the islands and submerged reefs database from Bourdin et al. (2025), which was consolidated from the General Bathymetric Chart of the Oceans (GEBCO) database (GEBCO Bathymetric Compilation Group, 2022), the high-resolution global island database (Sayre et al., 2019, 2020), and the submerged reef database from Messié et al. (2022). We used the modeled daily surface currents data for the detection algorithm (i.e. global ocean ensemble physics reanalysis products distributed by Copernicus Marine Services; European Union-Copernicus Marine Service, 2019). As in previous studies (Messié et al., 2022; Bourdin et al., 2025), we define the background ocean (BO) reference zone associated with each IME zone as an area equal in size to the corresponding IME zone but located outside of it, closest to the island or submerged reef mask. We then extracted bio-optical properties derived from satellite data for all IMEs and their associated BO areas. To identify consistent patterns across the South Pacific Subtropical Basin and all seasons sampled, we performed a principal component analysis (PCA) using the average bio-optical properties of all 2025 individual IME realizations and their associated BO areas detected in the four case study regions along the six-month periods. Only variables derived from satellite measurements and assimilative models were used in this analysis to ensure sufficient data coverage (i.e. [Chla], b_{bp}, $[Chla]/[C_{phyto}]$, SST, MLD, Φ_{Sat}, and η'). Additionally, we identified in situ measurements located within IMEs contours to validate patterns we observed in satellite data and complement the interpretation with information on pigment ratios as proxies for phytoplankton community composition, as well as macronutrient and iron concentrations.

3 Results and Discussion

Six-month-long time-series data highlighted relatively strong seasonal variability in IME magnitude (Bourdin et al., 2025), but also showed consistent contrasts between properties of IME and BO zones across the longitudinal gradient. IMEs associated with the studied islands were consistently characterized by higher average $[Chla]/[C_{phyto}]$, and lower averages of Φ_{Sat} and η' relative to BO (Fig. 2). These results are consistent with the hypothesis that IMEs are areas where nutrient limitation is alleviated compared to the background ocean.

The distance between the IME and BO centroids along the first principal component, is larger in the western basin (i.e. Samoa, and Fiji and Tonga case studies) than in the eastern basin of the SPSG (i.e. Rapa Nui and Society Islands case studies; Fig. 2), suggesting that iron enrichment in IME zones is higher in the western Pacific compared to eastern basin. This difference may be due to higher concentration of active shallow and deep hydrothermal vents located around islands and seamounts in the western Pacific basin, which serve as substantial sources of iron in this region (Bonnet et al., 2023; Guieu et al., 2018). Another key oceanographic difference between the eastern and western SPSG is the depth of the nutricline, which is generally deeper in

https://doi.org/10.5194/egusphere-2025-4261
Preprint. Discussion started: 20 October 2025

the east, particularly around Rapa Nui (∼150-220 m in the eastern basin versus 70-80 m in the western basin; Longhurst, 2007; Raimbault et al., 2008). Consequently, wind-driven divergence in the eastern basin is more likely to upwell nutrient-depleted water from above the nutricline. In addition, for a given wind speed, the magnitude of upwelling and macronutrient enrichment is expected to be stronger around large islands with long and continuous coastlines, such as Viti Levu in the Fiji archipelago, than around isolated small islands like Rapa Nui or archipelagos of smaller islands such as the Society Islands (De Falco et al., 2022).

The Society Islands, Samoa, and Fiji-Tonga IMEs were characterized by reduced η' relative to their respective BO zones (Fig. 2). Two phases of IME occurred around Rapa Nui. The first phase, the austral winter phase, was characterized by higher vertical mixing (i.e. deeper MLD), lower SST, and no apparent correlation of the IME with η'. The second phase, the austral summer phase, was characterized by shallower MLD, higher SST, and correlations between IME and lower macronutrient stress. The points corresponding to the austral winter phase are distinct from the austral summer phase, and exhibit similar properties to the Society Islands' IME (Fig. 2). Rapa Nui is located 10 degrees south of Tahiti, just at the border of a strong SST latitudinal gradient visible south of Rapa Nui in the video supplements (or at Bourdin, 2025), suggesting that Rapa Nui's IME is characterized by different water mass properties than Tahiti during the austral winter.

https://doi.org/10.5194/egusphere-2025-4261
Preprint. Discussion started: 20 October 2025

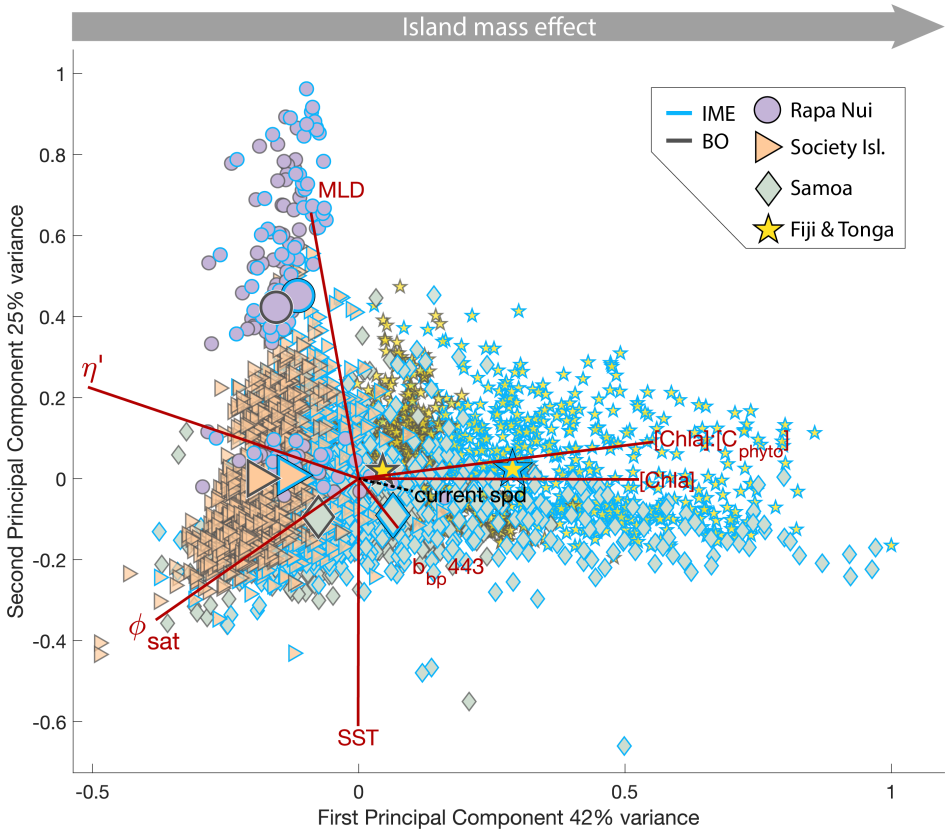

Figure 2. Principal component analysis of average chlorophyll *a* concentration ([Chla]), backscattering coefficient at 443 nm ($b_{bp}443$), ratio of [Chla] to phytoplankton carbon ($[Chla]/[C_{phyto}]$), iron stress index (Φ_{Sat}), macronutrient stress index (η'), mixed layer depth (MLD), and sea surface temperature (SST) of all individual IME (blue outline) and background ocean (BO, black outline) zones detected in each 8-day period along the six-month time-series in all of the four case studies (N = 2025 realizations of IMEs). Small markers represent all individual IME and BO averages for each studied region, and larger markers represent their centroids. Surface current speed ('current spd') is overlaid in black as a supplementary variable.

All IMEs, except Rapa Nui's, were characterized by moderate increases in b_{bp} at 443 nm ($b_{bp}443$) and therefore increases in phytoplankton biomass (Fig. 2). No consistent pattern in satellite b_{bp} in the IME was observed around Rapa Nui, but measurements from the continuous underway system show higher surface c_p660 values within all IME zones across the four case studies (Bourdin et al., 2025). Assuming in situ sampling periods are representative of the six-month time-series, the increase in biomass associated with Rapa Nui's IME was likely too low to be detected using satellite b_{bp} (due to high uncertainty in retrieval, see A3 Bisson et al., 2021). The ultra-oligotrophic ocean around Rapa Nui is largely dominated by picophytoplankton that are tightly coupled with their grazers, heterotrophic and pigmented nanoflagellates, which have similar generation times on the order of a day (Connell et al., 2020; Livanou et al., 2019; Yun-Chi et al., 2009). This tight coupling may have prevented an accumulation of phytoplankton biomass detectable from remote sensing around Rapa Nui.

https://doi.org/10.5194/egusphere-2025-4261
Preprint. Discussion started: 20 October 2025

In order to investigate the sources of nutrients associated with IME, we analyze incoming and outgoing transects around islands to identify markers of upwelling of deep nutrient-rich water to the surface. We also examined these transects to identify zones of minimum macronutrient or iron stresses corresponding to high concentrations, which would inform on the origin of enrichments.

3.1 IME and phytoplankton photophysiology

The IME detected around Fiji was characterized by a surface integrated [Chla] enhancement of about 55 t m^{-1} and covered a surface of about 500,000 km^2 at the time of sampling (Bourdin et al., 2025). The increase of c_p660 (i.e. proxy for particulate organic carbon concentration; Gardner et al., 2006; Behrenfeld and Boss, 2006) by a factor of ∼15 observed over a ∼10 km transect approaching shore, west of the archipelago, suggests the [Chla] enhancement in the IME was associated with a significant increase in phytoplankton biomass (Bourdin et al., 2025, Fig. 6). A distinct and synchronized decrease in SST and SSS on May 30^{th} ∼10:00 UTC indicated a change of water mass measured along the inbound transect to the Fiji archipelago (Fig. 3 B. and C.). This change in water mass was associated with a gradual decrease in the proportion of photoprotective carotenoids ($[PPC]/[Chla]$) and a gradual increase in $[Chla]/[C_{phyto}]$ (Fig. 3 D and E). These two independent metrics of light acclimation had opposite trends, suggesting that the same forcing was impacting both of them. The proportion of $[PPC]$ can be modulated by phytoplankton in response to changes in ambient light to prevent intracellular photo-oxidative stress (Caferri et al., 2022). Likewise, the proportion [Chla] to $[C_{phyto}]$ is modulated in response to light conditions, resulting in phytoplankton cells at the surface of the ocean characterized by lower $[Chla]/[C_{phyto}]$ and higher $[PPC]/[Chla]$ than cells residing at depth, where low levels of ambient light require more [Chla] for photosynthesis but also cause less photo-oxidative stress, therefore requiring lower concentrations of photoprotective pigments. The lowest SST and $[PPC]/[Chla]$ and the highest $[Chla]/[C_{phyto}]$ of the inbound transect were measured just adjacent to the island's shelf break. These parameters changed suddenly when *Tara* sailed across the shelf through the Navula Passage west of the Fiji archipelago (i.e. coastal zone Fig. 3 D and E). Together, these synchronized trends observed with four independent measurements are consistent with the presence of an upwelling event that occurred in a ∼170 km wide band near the coast west of Viti Levu at the time of sampling. [PPC]/[Chla] was marginally lower, and $[Chla]/[C_{phyto}]$ was marginally higher, but overall heterogeneous in this IME detected in the outbound transect, suggesting a weaker upwelling of cells that are acclimated to low light to the surface than in the inbound transect. The surface currents were flowing southward at the time of sampling and the week before, suggesting that the IME detected south of Fiji was located downstream of Fiji. Similar signals were detected southwest of Rapa Nui and Tahiti-Mo'orea, along the outbound transects, indicating that sub-surface phytoplankton populations were recently upwelled to the surface (see Appendix B). In contrast, there is no clear evidence that upwelling occurred around Samoa at the time of sampling (see Appendix B). Indeed, in situ data show that the IME advected offshore had the same characteristics as the water mass closest to shore (that is, higher SST, lower SSS, and no significant differences in $[PPC]/[Chla]$ and $[Chla]/[C_{phyto}]$; see Appendix B), therefore the main source of nutrient in Samoa's IME were likely associated with terrigenous processes.

We extracted satellite estimates of [Chla], $[Chla]/[C_{phyto}]$, and SST along the ship track (i.e. dashed line Fig. 3) to assess if satellite-based estimates can also inform us about processes involved in IME. Although satellite-derived [Chla] and SST

https://doi.org/10.5194/egusphere-2025-4261
Preprint. Discussion started: 20 October 2025

closely matched the magnitude of in situ underway measurements, the satellite $[Chla]/[C_{phyto}]$ values along the ship track were consistently lower than those estimated from in situ underway data. Satellite [Chla] and SST were nudged to agree with in situ underway estimates across the Pacific Ocean (see method 2.5 and Bourdin et al., 2025), however b_{bp} was not, due to the low correlation between in situ and satellite data (see method 2.5). This suggests that the Quasi-Analytical Algorithm (QAA; Lee et al., 2002, 2009) we used to invert b_{bp} from R_{rs} may not perform well in these ultra-oligotrophic regions since all b_{bp} measurements used to develop this inversion algorithm are higher than the in situ b_{bp} of the BO zones we measured in these regions ($b_{bp}443 < 0.001m^{-1}$). Moreover, b_{bp} inverted from satellite data using QAA was shown to be overestimated in these regions when compared to b_{bp} estimated from profiling floats (when $b_{bp}700 < 0.001m^{-1}$; Bisson et al., 2021). In this case, an overestimation of the satellite b_{bp} would lead to an underestimation of $[Chla]/[C_{phyto}]$ and would explain the observed discrepancies between in situ and satellite estimates. Despite this difference in magnitude, the spatial variability of $[Chla]/[C_{phyto}]$ estimated from satellite data captured the same spatial variability as the situ estimates, although slightly smoother due to the 8-day time binning applied (i.e. dashed line Fig. 3). These results show the potential of satellite data to discriminate between biomass enhancement and signatures of coastal upwellings around islands and improve the mechanistic understanding of IME. However, it requires minimizing the satellite temporal binning to capture short-lived events that would otherwise be undetectable.

https://doi.org/10.5194/egusphere-2025-4261
Preprint. Discussion started: 20 October 2025

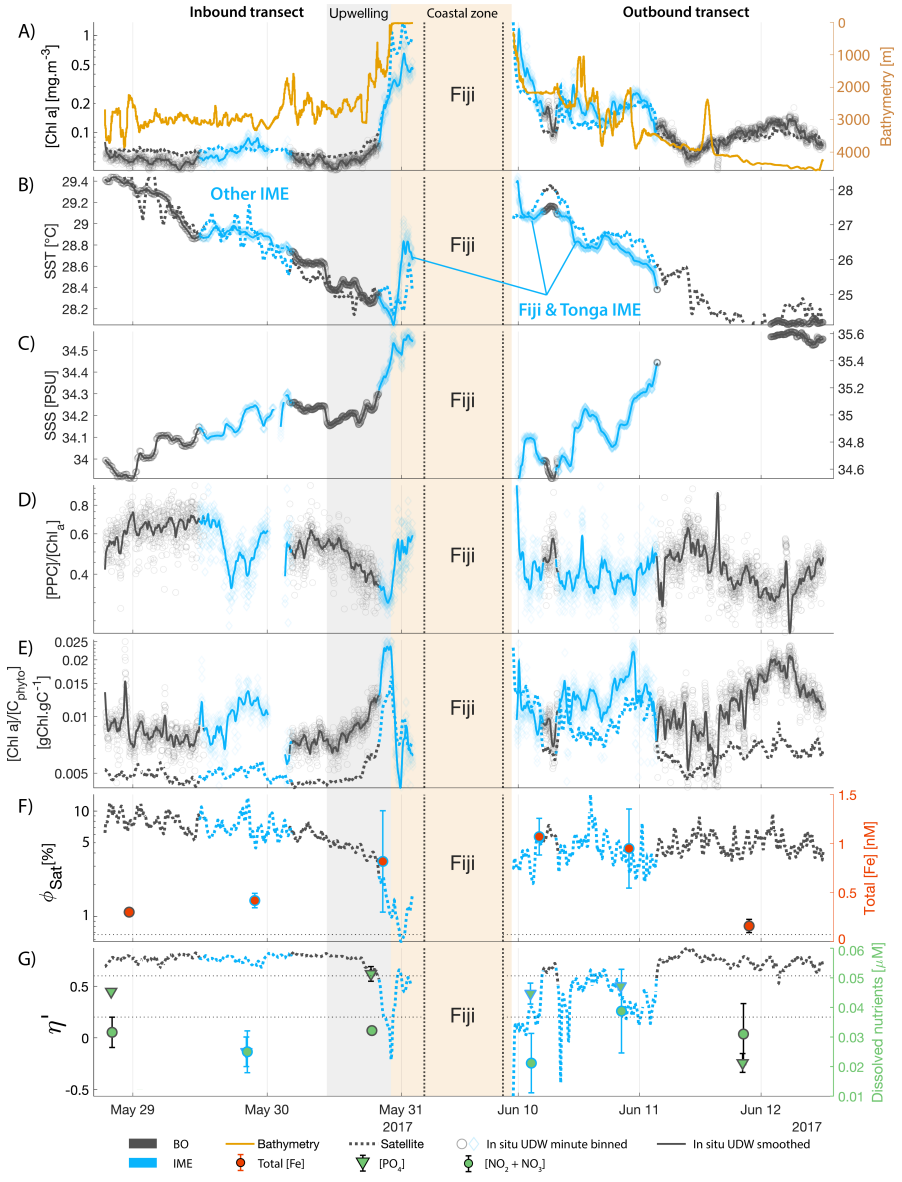

Figure 3. Underway data measured during the inbound (left panels) and outbound (right panels) transects around Fiji and their satellite counterparts, when available. **A)** Chlorophyll a concentration ([Chla]) and bathymetry, **B)** sea surface temperature (SST), **C)** sea surface salinity (SSS), **D)** Photo-protective carotenoids proportion ($[PPC]/[Chla]$), **E)** [Chla] to phytoplankton carbon ratio ($[Chla]/[C_{phyto}]$), **F)** fluorescence quantum yield (Φ_{Sat}; iron stress index) and total iron concentration measured at sampling stations, and **G)** macronutrient stress index (η') and macronutrient concentrations measured at sampling stations. The blue points show in situ data falling in IME zones detected on the overlapping 8-day satellite composite (BO = black circle, IME = blue diamond). The points show the minute-binned underway data, and the solid lines represent the underway data smoothed with a 2h low-pass digital filter. The gray shaded area highlights the coastal upwelling zone, and the beige shaded area highlights the transect over shallow waters (< 100 m depth).

https://doi.org/10.5194/egusphere-2025-4261
Preprint. Discussion started: 20 October 2025

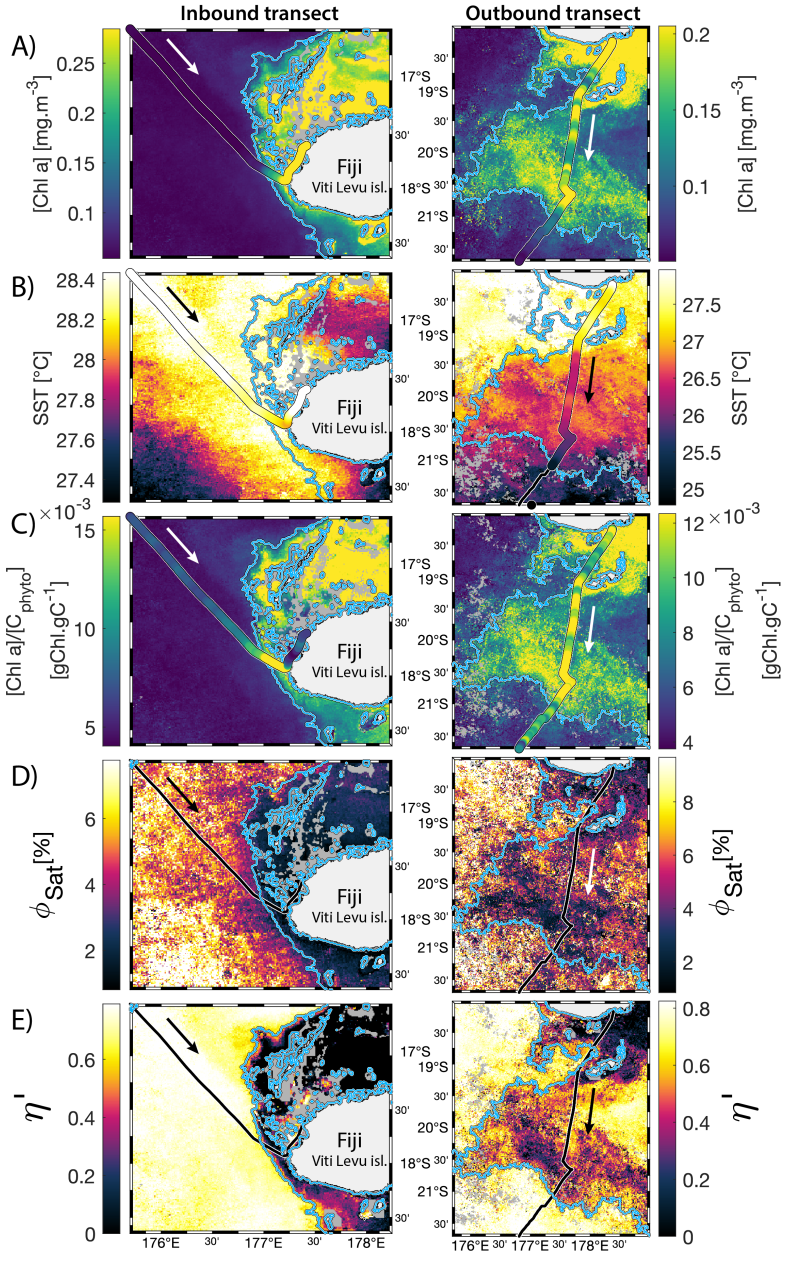

Figure 4. 8-day median satellite maps zoomed on the inbound (left-hand-side panels) and outbound transects (right-hand-side panels) around Fiji (arrow shows sailing direction). The blue contour delineates the island mass effect zone detected from satellite chlorophyll *a* concentration ([Chla]). In situ underway measurements are overlaid on the satellite map if the same variable was measured from satellite estimates and the underway system. **A)** [Chla], **B)** sea surface temperature (SST), **C)** [Chla] to phytoplankton carbon ratio ($[Chla]/[C_{phyto}]$), **D)** fluorescence quantum yield (ϕ_{Sat}), and **E)** macronutrient stress index (η').

https://doi.org/10.5194/egusphere-2025-4261
Preprint. Discussion started: 20 October 2025

3.2 IMEs and spatial pattern in phytoplankton nutrient physiology

The satellite map around Fiji shows that the IME patch is characterized by higher $[Chla]/[C_{phyto}]$, as well as lower Φ_{Sat} and η' indices, suggesting enrichment in iron and macronutrients, and enhanced upwelling of subsurface population within the IME relative to BO (Fig. 4 and 3). Total iron concentrations measured at the sampling stations were the highest in Fiji's IME (Fig. 3). The iron stress index (Φ_{Sat}) decreased along the inbound transect, with the steeper decrease detected over the island shelf, past the detected upwelling zone. This suggests that iron enrichment was driven by processes associated with the archipelago itself (e.g. leaching from sediments, runoff, or shallow hydrothermal activity) rather than an upwelling event (Fig. 3). The macronutrient stress index (η') also decreased along the inbound transect with a minimum coinciding with the upwelling signal and higher values over the shelf area, suggesting that the upwelling west of Fiji was the main source of macronutrients to the euphotic zone along this transect. η' was also consistently lower in the IME of the outbound transect relative to the BO, suggesting a macronutrient enrichment across Fiji-Tonga's IME.

The concentrations of nitrogen and phosphate were, in general, higher at coastal stations compared to offshore stations (advected IME and BO; Fig. C1), indicating that terrigenous inputs, through runoff and organic macronutrient production in coral reefs, were a significant source of macronutrients. These concentrations were rarely higher in the advected IME compared to the BO. For example, despite a strong enrichment in nitrogen and phosphate in the coastal IME of Fiji (Fig. C1), concentrations are already low at the closest station to the island shore downstream of Fiji (Fig. B1), suggesting that a large proportion of these macronutrients were rapidly depleted relatively close to shore. The upstream water masses, which were impacted by local coastal upwelling and terrigenous processes, were probably diluted south of Fiji through mixing with the oligotrophic BO and modified by local upwelling and downwelling associated with positive and negative vorticity (De Falco et al., 2022). Interactions of currents with islands and seamount topography can also result in doming isopycnals and increased vertical mixing downstream of islands (Heywood et al., 1990; De Falco et al., 2022). We hypothesize that this enhanced vertical mixing could have sustained a small influx of macronutrients to the euphotic zone in the IME, as shown by the consistently lower macronutrient stress (i.e. $\eta' \leq 0.6$) in the IME zone of the outbound transect. Although phosphate concentrations measured at stations located in the IME of Fiji-Tonga were consistently higher than in the BO, nitrogen concentrations were lower at the offshore station closest to Fiji on the outbound transect (Fig. B5). Phytoplankton biomass was higher at this station, particles were larger on average, and pigment ratios were characteristic of a higher proportion of diatoms, suggesting that nitrogen (nitrate + nitrites) could have been quickly consumed by the phytoplankton community (Fig. B5 and 5).

Relatively high total iron concentrations were detected downstream of Fiji (south), further away from the coast, yet Φ_{Sat} increased rapidly along the outbound transect. Automated microscopy analyses show a high prevalence of *Trichodesmium* spp. in the IME zone along the outbound transect (Mériguet et al., 2024a, b), and this bloom was visible to the naked eye during sampling (Bourdin, personal observation). Iron requirements vary between phytoplankton taxa; for example, *Trichodesmium* spp. is known to have higher iron requirements compared to other taxa (Berman-Frank et al., 2001a). Furthermore, there is a high inter-species variability in the ratio of chlorophyll fluorescence to chlorophyll concentration (i.e. FChl / [Chla]) (Petit

https://doi.org/10.5194/egusphere-2025-4261
Preprint. Discussion started: 20 October 2025

et al., 2022; Roesler et al., 2017), which could impact the estimation of Φ_{Sat} and explain the difference in the relationship between the total iron concentration and Φ_{Sat} at these stations. *Trichodesmium* spp. colonies are composed of 'bright cells' that have twice the basal fluorescence of other cells in a non-diazotrophy state and three times as many when in a diazotrophy state (Berman-Frank et al., 2001b; Küpper et al., 2008). The bloom of *Trichodesmium* spp. observed on the outbound transect at sampling stations where the total iron concentration was an order of magnitude higher than in BO indicates that diazotrophy was likely occurring in this bloom. *Trichodesmium* spp. diazotrophy can be a significant nitrogen source in the western subtropical Pacific Ocean, where the influx of nitrogen into the euphotic zone from depth is limited due to low mesoscale mixing (Shiozaki et al., 2014). We did observe an increase in the concentration of dissolved inorganic nitrogen (nitrate + nitrite) coinciding with the highest *Trichodesmium* spp. biomass in the advected IME zone (see microscopy count in Mériguet et al., 2024a, b) that could indicate a biogenic input. Together, these observations suggest high diazotrophic activity in the IME zone along the outbound that could explain the observed high Φ_{Sat} values in an iron-enriched zone. In addition, not all iron forms in the measured total iron are bioavailable and, therefore, must be interpreted with caution in the context of the physiological response of phytoplankton to iron availability.

For the three other case studies, total iron concentrations generally increased while Φ_{Sat} decreased. The magnitude of the increase in total iron concentration shows a longitudinal gradient with the lowest increase around Rapa Nui and the highest increase around Fiji (Fig. 3, B1, B3, and B5). This observation is consistent with the gradient in iron enrichment associated with IMEs detected across the SPSG. Fiji and Tonga's IMEs were, on average, characterized by the largest difference in Φ_{Sat} between the IME and the BO zone, and the smallest difference was observed for Rapa Nui's IME (Fig. 2). The decrease in η' was more marginal in the other three case studies, particularly around Rapa Nui and the Society Islands, where it only decreased significantly at the border of the coastal zone. At this distance from shore, the 8 km spatial resolution of the MLD product used for the calculation of η' is likely too coarse to capture the complexities of coastal submesoscale dynamics. Similarly, macronutrient concentrations around Fiji were generally higher in coastal zones, but declined sharply with increasing distance from the island (Fig. C1). This pattern suggests that macronutrients supplied by terrigenous and reef-associated processes are rapidly consumed by phytoplankton near the shore. This observation supports the hypothesis of Messié et al. (2020), who proposed that nitrogen is quickly utilized in coastal waters by phytoplankton taxa with higher nitrogen uptake capacity, such as diatoms. Consistently, the spatial distribution of pigment markers in this study indicates that the relative concentration of diatoms increased most strongly near the island shelf (see section 3.3; Fig. 5 and D1).

The data collected on board during the inbound transect to Rapa Nui show that the IME detection algorithm from satellite only captured the strongest [Chla] increase near-shore, missing the marginal increase that is highlighted in the gray shaded area (Fig. B1). The strong latitudinal SST front associated with the highest [Chla] located south of Rapa Nui shifted north toward Rapa Nui at this period, masking the increase in [Chla] due to IME, and caused the iterative IME detection algorithm to stop before the contour of [Chla] was low enough to encompass the entire IME zone (see video of time series in Bourdin, 2025). Interestingly, this slight increase in [Chla] in this zone was not associated with a detectable increase in c_p660 (see Appendix D Fig. D1 in Bourdin et al., 2025). This suggests that despite evidence of iron enrichment (lower Φ_{Sat} and higher total iron concentrations) and reduced macronutrient stress (lower η') compared to the rest of the inbound transect, there was

https://doi.org/10.5194/egusphere-2025-4261
Preprint. Discussion started: 20 October 2025

no detectable biomass increase in this zone. As discussed previously, any increase in picophytoplankton biomass is rapidly consumed in this pico-sized dominated environment, often preventing any detectable biomass accumulation using in situ or remotely sensed bio-optical proxies, despite increased nutrient availability.

3.3 Characteristics of phytoplankton communities from bio-optical signals

Bio-optical proxies of community composition associated with IMEs showed distinct patterns between the western and eastern South Pacific basins. Suspended particles (i.e. mean cell size) were larger in the IME in the western South Pacific basin (i.e. Samoa and Fiji), while the advected IME and coastal IME were characterized by smaller average particle size than the BO in the eastern South Pacific Ocean (i.e. higher γ_{cp} in Rapa Nui and Society islands' IMEs; Appendix D and Fig. D1). The proportion of $[PSC]$ (i.e. $[PSC]/[Chla]$, indicative of relative concentration of diatoms; Kramer and Siegel, 2019) was higher in the coastal IME in the western Pacific basin (Fig. 5, Appendix D and Fig. D1). The concentration of chlorophyll *b* and chlorophyll *c* relative to [Chla] ($[Chlb]/[Chla]$ and $[Chlc]/[Chla]$, indicative of green and red algae) was higher in the coastal IME of Samoa and both the advected and coastal IMEs of Fiji-Tonga (Appendix D and Fig. D1). Similarly, the relative absorption of phycoerythrin ($a_{gauss}550/a_{gauss}676$), indicative of cyanobacteria relative concentration, was higher in the coastal IME of Samoa and both the advected and coastal IMEs of Fiji-Tonga (Appendix D and Fig. D1). In contrast, the proportion of all accessory pigment groups normalized to [Chla] decreased in the IME of the Society Islands compared to the BO. This may be due to decreased pigment packaging since the cells were, on average, smaller in the IME relative to the BO in this case (Appendix D and Fig. D1).

To investigate the impact of the different enrichment mechanisms on phytoplankton community composition, we focus on the transects of the Fiji–Tonga case study. Suspended particles were larger on average (i.e. lower γ_{c_p}) and accessory pigments concentrations normalized by [Chla] were higher in the IME of Fiji-Tonga compared to the BO zones (Fig. 5). Both mean particle size and accessory pigments concentrations increased sharply in the inbound transect and gradually decreased in the outbound transect when crossing the IME zones located on the downstream side of the archipelago (Fig. 5). These observations suggest that the strongest change in phytoplankton community composition observed along this transect occurred close to the island shelf (Fig. 5). The relative concentrations of accessory pigments did not all increase at the same distance from shore, suggesting a succession of dominant phytoplankton groups along the gradient from the background ocean to the island coast (Fig. 5). Using a Lagrangian particle tracking model and MERCATOR Ocean daily surface current products, we estimated that the time of advection for a given water parcel from the coastal area around Fiji to the BO zone is more than 30 days, a period sufficiently long for an ecological succession in the phytoplankton community to occur (outbound transect in Fig. 5). $[PSC]/[Chla]$ was particularly higher near shore and decreased relatively quickly along the outbound transect, indicating that the proportion of diatoms may have been higher in coastal waters compared to the rest of the IME and BO zones sampled (Fig. 5). The proportion of chlorophyll *b* and chlorophyll *c* relative to [Chla] increased as soon as *Tara* entered Fiji's IME zone in the inbound transect and remained higher across the IME zone sampled on the outbound transect relative to the BO, indicating that the proportions of other red algae and green algae remained higher further south of Fiji in the IME zone (Fig. 5). Similarly,

https://doi.org/10.5194/egusphere-2025-4261
Preprint. Discussion started: 20 October 2025

the proportion of phycoerythrin, indicative of cyanobacteria, also remained higher further south of Fiji, consistent with the *Trichodesmium* spp. bloom in the outbound transect observed using automated microscopy (Mériguet et al., 2024a, b).

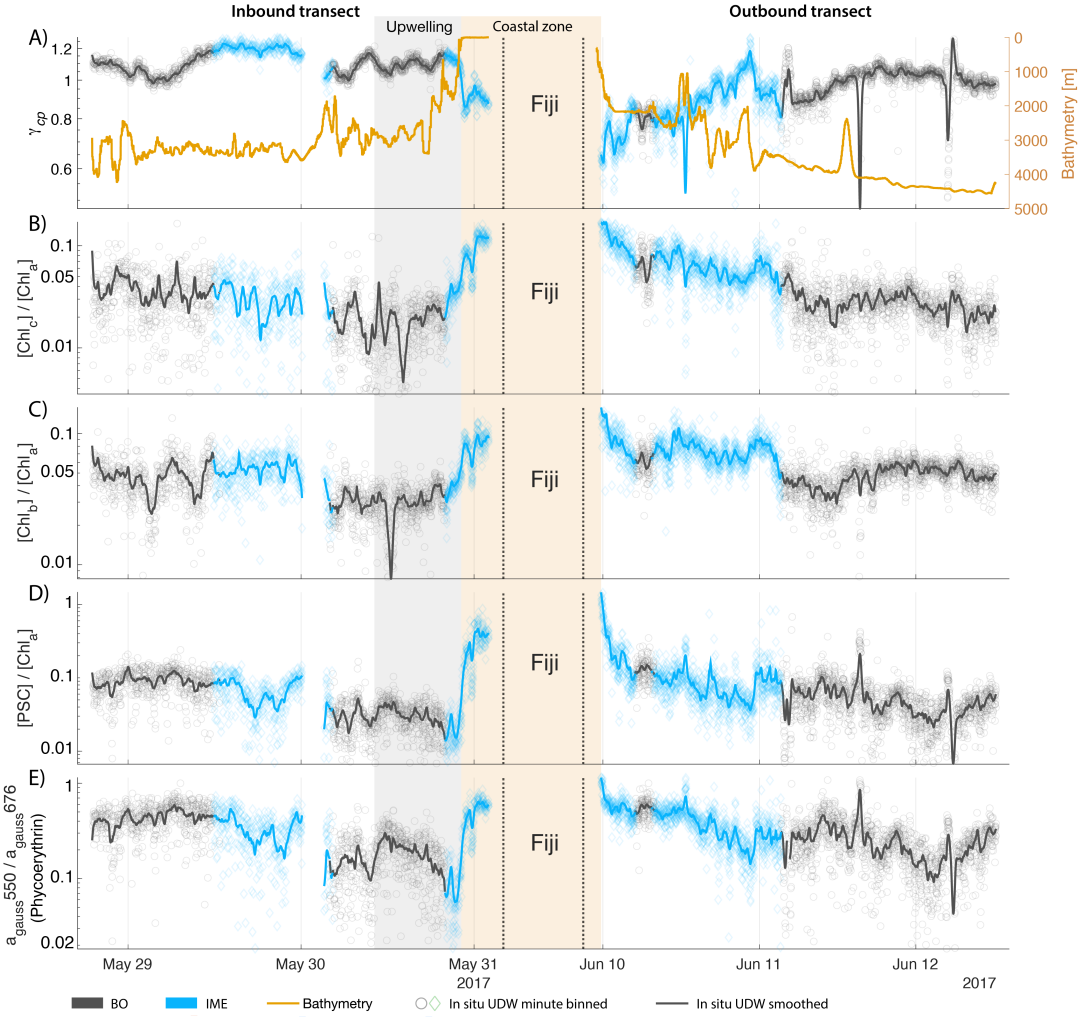

Figure 5. Underway bio-optical proxies for changes in community composition measured during the inbound (left panels) and outbound (right panels) transects around Fiji. **A)** mean particle size index (γ_{c_p}), **B)** Chlorophyll *c* normalized by [Chla] ($[Chlc]/[Chla]$), **C)** Chlorophyll *b* normalized by [Chla] ($[Chlb]/[Chla]$), **D)** photosynthetic carotenoids normalized by [Chla] ($[PSC]/[Chla]$), and **E)** Phycoerythrin particulate gaussian absorption at 550 nm normalized by [Chla] particulate gaussian absorption at 676 nm ($a_{gauss}550/a_{gauss}676$). The blue points show in situ data falling in IME zones detected on the overlapping 8-day satellite composite (BO = black circle, IME = blue diamond). The points show the minute-binned underway data, and the solid lines represent the underway data smoothed with a 2h low-pass digital filter. The gray shaded area highlights the coastal upwelling zone, and the beige shaded area highlights the transect over shallow waters (< 100 m depth).

https://doi.org/10.5194/egusphere-2025-4261
Preprint. Discussion started: 20 October 2025

3.4 Temporal dynamics

The IME detected around Fiji-Tonga, increased in surface and surface-area integrated [Chla] from the end of February to early May 2017, when it covered more than one million square kilometers. The impacted area then decreased between May and the end of August 2017 (Fig. 6.B). The difference in Φ_{Sat} between the IME and the BO ($\Delta\Phi_{Sat}$) was consistently negative, indicating a lower phytoplankton physiological stress and a net enrichment in iron in the Fiji-Tonga IME relative to the BO, especially at the beginning of the time-series, during the expanding phase of the IME (i.e. February to May). Φ_{Sat} in the IME decreased overall during the studied period, suggesting an increase in iron enrichment in the IME. Given that the difference in Φ_{Sat} between the IME and BO decreased (i.e. $\Delta\Phi_{Sat}$ approached 0), the net iron enrichment associated with the IME relative to the BO decreased over this period despite an increase in iron enrichment in the IME. Therefore, the iron stress in the BO decreased more than the iron stress in the IME over the period studied, suggesting that the processes controlling phytoplankton iron stress in the IME had less seasonal variability than those in the BO. Phytoplankton communities in the IME were not experiencing stress due to macronutrient limitation during the expanding phase of the IME (i.e. February to May with $\eta' < 0.2$) but started to experience a moderate stress three weeks before the end of the expansion phase of the bloom (i.e. $0.2 < \eta' \leq 0.6$). Φ_{Sat} and η' were significantly lower in Fiji-Tonga's IME relative to the BO, even during bloom demise, suggesting that top-down controls, such as grazing, contributed to the bloom demise before the iron and macronutrients were fully depleted from the euphotic zone in the IME.

Samoa's IME was characterized by two important phytoplankton biomass accumulation phases (i.e. blooms) over the period studied, highlighted by two distinct IME-surface-area integrated [Chla] peaks around November 9th and December 19th 2016. Interestingly, in Samoa's IME, iron and macronutrient stress did not decrease before and during the initiation of the first of these two blooms and were consistently lower in the IME compared to the BO along the entire time series, which suggests that the occurrence of the first bloom in Samoa's IME was not only triggered by bottom-up processes such as macronutrient and iron enrichment. This first bloom only initiated after being advected offshore and detached from the coastal IME of Samoa, which coincided with the dilution of coastal waters into the BO. This dilution may have decreased the encounter rate between grazers and their prey, reducing the grazing pressure, while the high levels of macronutrients and iron advected within this water mass maintained phytoplankton growth rate, allowing for positive accumulation of phytoplankton biomass (such as hypothesized in Lehahn et al., 2017; Bourdin et al., 2025). This hypothesis is also supported by the similarities in physical properties of Samoa's advected IME and the ones of its coastal IME (i.e. warmer and fresher than the BO south of Samoa; Fig. B5 and B6), which suggest that the water mass advected offshore had a coastal origin (see section 3.1 and Appendix B).

While these results suggest continuous enrichments in iron and macronutrients in IME zones in the western South Pacific Ocean, the results are more contrasted in the eastern South Pacific Ocean where Φ_{Sat} and η' in IME areas are often not significantly lower than in the BO (illustrated by $\Delta\Phi_{Sat} + SEM^f_{\Delta\Phi_{Sat}} > 0$ or $\Delta\eta' + SEM^f_{\Delta\eta'} > 0$; Appendix E, Fig. E1, and Fig. E2).

https://doi.org/10.5194/egusphere-2025-4261
Preprint. Discussion started: 20 October 2025

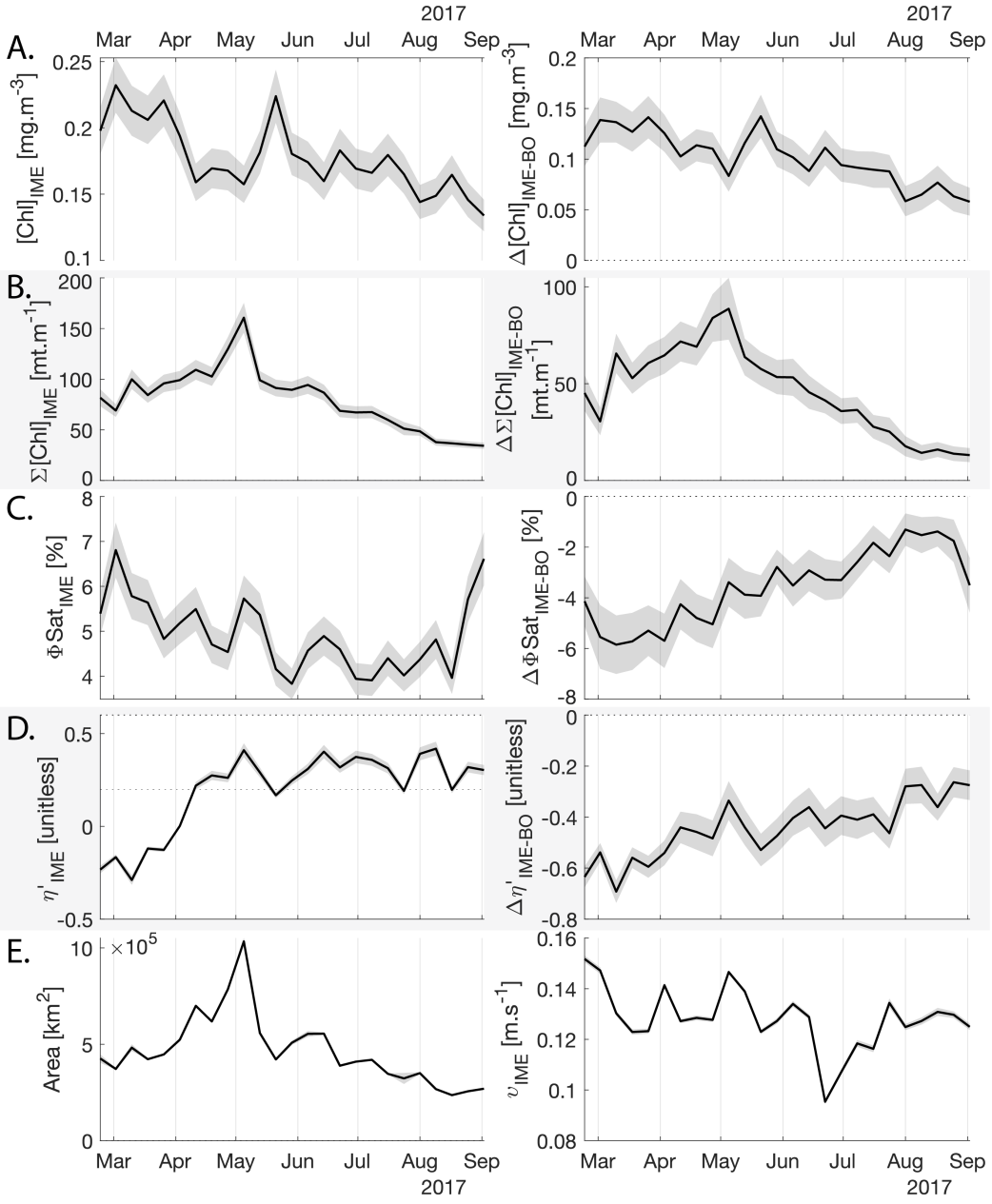

Figure 6. Six-month-long time series of satellite-derived IME properties of the IME zone detected around Fiji and Tonga archipelagos combined. **A, B, C, and D left panels**: Average of properties within the IME zones, **A, B, C, and D right panels**: Difference between properties within the IME zones and the background ocean (BO). **A row**: chlorophyll *a* concentration ([Chla]), **B row**: IME integrated [Chla] ($\sum[Chla]_{IME}$), **C row**: fluorescence quantum yield (ϕ_{Sat}), **D row**: macronutrient stress index (η'), **E left:** IME zone area (in km^2), **E right**: surface current velocity.

https://doi.org/10.5194/egusphere-2025-4261
Preprint. Discussion started: 20 October 2025

3.5 Relating IME properties to characteristics of islands

Although the four cases studied were sampled during different seasons, we detected a longitudinal gradient in the strength of the IME and its associated iron enrichment (i.e. from Rapa Nui to Fiji) in the SPSG. However, this longitudinal gradient should be interpreted with caution, as the size of the IME area is correlated with the size of islands (Fig. 7A, where Σ(30 m isobath area) is plotted against IME_{area}), highlighting that island size can be an important driver of IME magnitude.

https://doi.org/10.5194/egusphere-2025-4261
Preprint. Discussion started: 20 October 2025

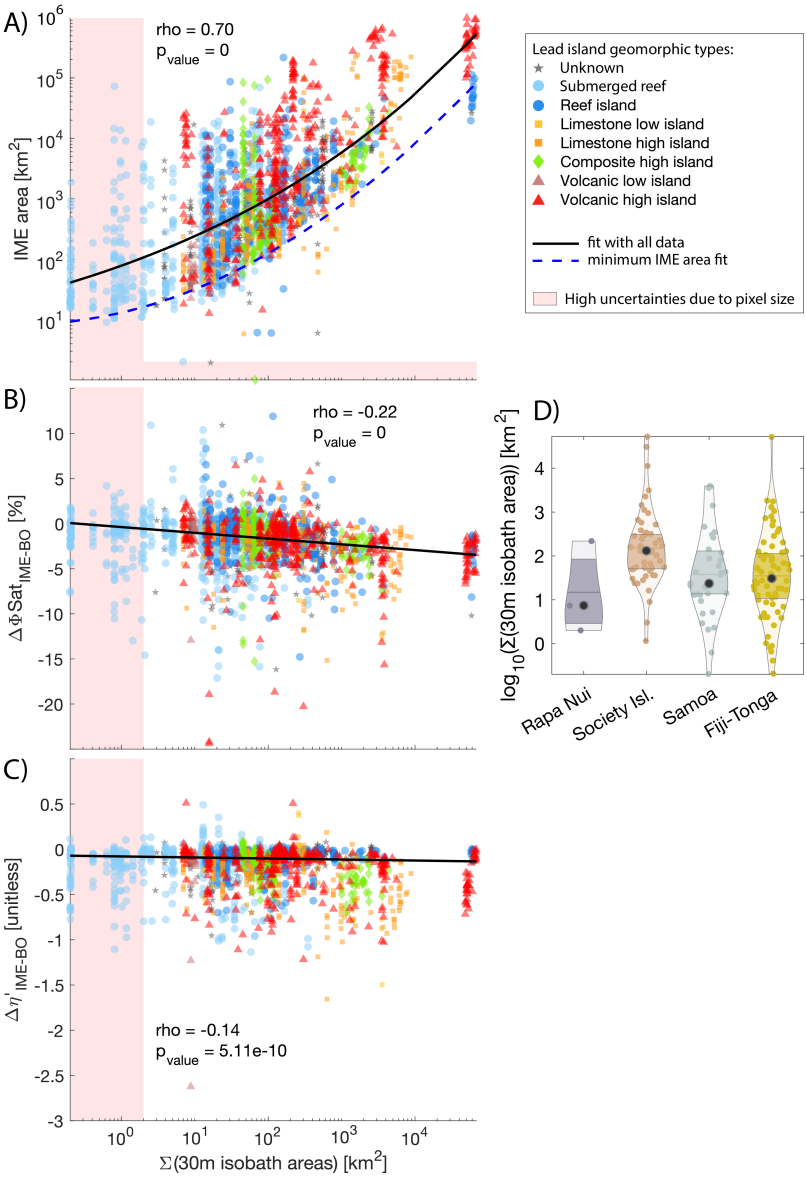

Figure 7. Relationship between the summed 30 m isobath areas of all islands and reefs associated with each individual IME and the IME area (A), the difference between average fluorescence quantum yield in IME and BO (B), the difference between average macronutrient stress index in IME and BO (C). The black solid line represents a robust second-order polynomial fit (A) and linear fits (B and C). The blue dashed line represents the second-order polynomial fit of the minimum IME area prediction (A). Different colors and marker shapes represent the different island/reef geomorphic types from the Nunn et al. (2016) island database. The shaded polygons represent high uncertainty areas due to pixel size. Subplot (D) represents the distributions of 30 m isobath areas of all islands contributing to IMEs in each region.

https://doi.org/10.5194/egusphere-2025-4261
Preprint. Discussion started: 20 October 2025

The Σ(30 m isobath area) is a good predictor of the potential minimum IME_{area} using a second-order polynomial model (i.e. dashed blue line in Fig. 7.A):

$$log_{10}(IME_{area_{min\ predicted}}) = 1.114 + 0.281X + 0.105X^2 \quad (7)$$

where $X = log_{10}(\Sigma(30m\ isobath\ area))$. Island size alone is not a good predictor of the strength and extent of the IME given the large range of IME area for a given Σ(30 m isobath area) (Fig. 7). Other factors related to the mechanisms of nutrient enrichment (that are independent of size), such as the stoichiometry of macronutrient and trace metal enrichment (due to different enrichment sources), phytoplankton community composition, and grazing pressure, also play an important role in determining the magnitude of the IME phenomenon.

The rank in the magnitude of the IME observed in Figure 2 (Fiji-Tonga > Samoa > Society Islands > Rapa Nui) does not correspond to the rank of the island/reef area contributing to the IME of each region (Fig. 7 D). For example, the total 30 m isobath areas of all islands and reefs that contributed to the IMEs in the Society Island region are larger on average than the total 30 m isobath areas of Samoa and Fiji-Tonga (Fig. 7 D). Island/reef size is represented here as the sum of all 30 m isobaths associated with an IME, which in the case of the Society Islands region, encompasses the Society Islands themselves, but also the Tuamotu archipelago, which is composed of 76 islands and atolls, some of which are among the largest atolls on the planet (e.g. Rangiroa covering 1640 km^2). Their land area relative to their 30 m isobath area is very small, therefore, the terrigenous inputs of these coral reef atolls are likely smaller in comparison to those of the large high islands of Viti Levu and Vanua Levu of Fiji's archipelago. Moreover, we hypothesize that islands of different geomorphic types may have different stoichiometries of macronutrient and iron enrichment. For example, volcanic islands are known to be sources of iron in the water column (Bonnet et al., 2023; Guieu et al., 2018), thus their IMEs may have, on average, higher $\Delta\Phi_{Sat_{IME-BO}}$ than the IMEs located around coral atolls. Our results, however, do not show clear trends between the geomorphic types of islands and their associated IME area or nutrient stress (Fig. 7). The lack of a clear trend may result from the multiple sources of variability inherent to this study (e.g., seasonal variability, regional variability in oceanographic conditions, variability in responses of different phytoplankton assemblages to macronutrient and iron enrichment), which could mask the signal. Although characterized by weak correlations, the iron and nutrient enrichments associated with IMEs increased with larger reef/islands, which is illustrated here by the negative correlation between Σ(30 m isobath area) and $\Delta\Phi_{Sat_{IME-BO}}$ and $\Delta\eta'_{IME-BO}$.

4 Conclusions

In this study, we used a combination of satellite-derived physiological stress markers and in situ optical data from an underway system to elucidate the links between IME, phytoplankton physiology, and community composition on the scale of the subtropical basin of the South Pacific. To our knowledge, such an endeavor has never been done.

Each of the four case studies exhibited unique spatial and temporal dynamics of IME (see result summary Table 4), yet in all cases we observed indications of a relaxation of iron stress in the IME relative to the regional surrounding ocean. Our results support the idea that islands or reefs also contribute to macronutrient enrichment from terrigenous origins, but unlike total iron

https://doi.org/10.5194/egusphere-2025-4261
Preprint. Discussion started: 20 October 2025

Table 4. Summary results of IME characteristics at the time of in situ sampling.

IME case studies	Rapa Nui	Society Isl.	Samoa	Fiji & Tonga
Biomass increase	yes	yes	yes	yes
Upwelling	no	yes	no	yes
Increased vertical mixing	yes	yes	no	yes
Iron enrichment	yes	yes	yes	yes
Iron stress decrease	yes	yes	yes	yes
Major source of iron	Terrigeneous processes	Terrigeneous processes	Terrigeneous processes	Terrigeneous processes
Macronutrient enrichment	not detectable	yes	yes	yes
Macronutrient stress decrease	not detectable	yes	yes	yes
Major source of macronutrients	n/a	Terrigeneous processes	Terrigeneous processes (run off)	Terrigeneous processes and upwelling
Particle size in coastal IME relative to BO	smaller	n/a	larger	larger
Particle size in advected IME relative to BO	no difference	smaller	no difference	larger
Change in community composition in coastal IME relative to BO	n/a	n/a	yes	yes
Change in community composition in advected IME relative to BO	n/a	yes	yes	yes

concentrations, which generally remain higher over entire IME zones, macronutrients are typically rapidly depleted by the time a given coastal water mass is advected into the open ocean. This rapid depletion is associated with higher proportions of diatoms near shore, which outcompete other phytoplankton for nitrate uptake (Litchman et al., 2007; Smith et al., 2019). The offshore IME water masses were associated with macronutrient enrichment originating from upwelling and vertical mixing processes in the western basin of the SPSG. Although detected in the eastern SPSG, these upwelling and vertical mixing signatures (i.e. low-light-adapted phytoplankton cells around islands) were generally not associated with significant macronutrient enrichment in the eastern SPSG, possibly due to the nutricline being deeper than in the western basin. The island and reef isobath area is a strong predictor of the minimum IME area and a weaker predictor of macronutrient and iron enrichment associated with IMEs; however, the high spatial and temporal variability of the IME area across the SPSG suggests that the magnitude of the IME phenomenon is strongly impacted by complex interactions between initial stocks of phytoplankton, bottom-up processes (i.e. stoichiometry of macronutrient and trace metal enrichment) and top-down controls (i.e. grazing pressure).

Based on these findings, we propose that IMEs represent naturally persistent nutrient enrichment experiments that could be studied to understand the impact of iron and macronutrient enrichment on natural plankton assemblages, net primary produc-

https://doi.org/10.5194/egusphere-2025-4261
Preprint. Discussion started: 20 October 2025

tion, and carbon export at the scale of entire basins. However, the uniqueness of each combination of factors that influence IMEs requires case-by-case studies, including temporal dynamics, to reveal specific underlying processes. In this context, the use of satellite data to detect upwellings, macronutrients, and iron enrichment to survey entire ocean basins is promising, especially with the recent deployment of the hyperspectral mission Plankton, Aerosol, Cloud, and Ocean Ecosystem (PACE) that can provide crucial information on phytoplankton community composition necessary to complement the interpretation of physiological signals. There is also a need to further validate these satellite-based estimates of iron and macronutrient stress, such as molecular markers from metatranscriptomic analyses, to enhance our confidence in the macronutrient and iron enrichment patterns deduced from remote sensing products and identify taxa-specific physiological responses.

Code and data availability. HPLC data are accessible from the BCO-DMO repository (https://doi.org/10.26008/1912/bco-dmo.889930.1, Bourdin and Karp-Boss, 2023). Iron and macronutrients concentration data are accessible at https://doi.org/10.5281/zenodo.6474974 (Lombard et al., 2023). In situ underway optical data can be accessed on the *Tara* Pacific SeaBASS repository (https://doi.org/10.5067/SeaBASS/TARA_PACIFIC_EXPEDITION/DATA001, Bourdin and Boss, 2016). The satellite binning software package used to create custom level-3 multi-satellite products from level-2 satellite data, to remove outliers, to nudge, and propagate uncertainties is accessible at https://doi.org/10.5281/zenodo.13376825 (Bourdin, 2024). Level-3 multi-satellite composites data, downloaded current data, the dynamic IME detection algorithm software, and its main outputs for each case study, including island databases for all region and their IME and BO masks, are available at https://doi.org/10.5281/zenodo.17156826 (Bourdin, 2025).

Author contributions. G.G., F.L., and E.B. designed and coordinated in situ sampling. G.B. collected and processed the in situ data. G.B. designed the satellite merging method and the dynamic IME detection method. G.B. and E.B. designed the macronutrient stress index. G.B., L.K.B., and E.B. assessed the method and wrote the original draft. All authors have read and reviewed the manuscript.

Competing interests. The authors declare no competing interests

Acknowledgements. Special thanks to the *Tara* Ocean Foundation, the R/V *Tara* crew, and the *Tara* Pacific Expedition Participants (Consortium, 2020). We are keen to thank the commitment of the following institutions for the financial and scientific support that made this unique *Tara* Pacific Expedition possible: CNRS, PSL, CSM, EPHE, Genoscope, CEA, Inserm, Université Côte d'Azur, ANR, agnès b., UNESCO-IOC, the Veolia Foundation, the Prince Albert II de Monaco Foundation, Région Bretagne, Billerudkorsnas, AmerisourceBergen Company, Lorient Agglomération, Oceans by Disney, L'Oréal, Biotherm, France Collectivités, Fonds Français pour l'Environnement Mondial (FFEM), Etienne Bourgois, and the *Tara* Ocean Foundation teams. *Tara* Pacific would not exist without the continuous support of the participating institutes. The authors also particularly thank Serge Planes, Denis Allemand, and the *Tara* Pacific consortium. We gratefully acknowledge Michael Behrenfeld for his insightful discussions on phytoplankton physiology and adaptation to nutrient availability. We particularly thank Seth G. John, Natalie R. Cohen, and Rachel L. Kelly for the analysis of iron concentration samples, Mireille Pujo-Pay for the analysis of

https://doi.org/10.5194/egusphere-2025-4261
Preprint. Discussion started: 20 October 2025

macronutrient samples, and Zoé Mériguet for the analysis of the automated microscopy data. This is publication number 48 of the *Tara* Pacific Consortium. This research has been supported by the NASA Ocean Biology and Biogeochemistry program (grant nos. 80NSSC20K1641, NNX13AE58G, and NNX15AC08G) and the National Science Foundation (grant no. 2025402).

https://doi.org/10.5194/egusphere-2025-4261
Preprint. Discussion started: 20 October 2025

Appendix A: Satellite variable computation

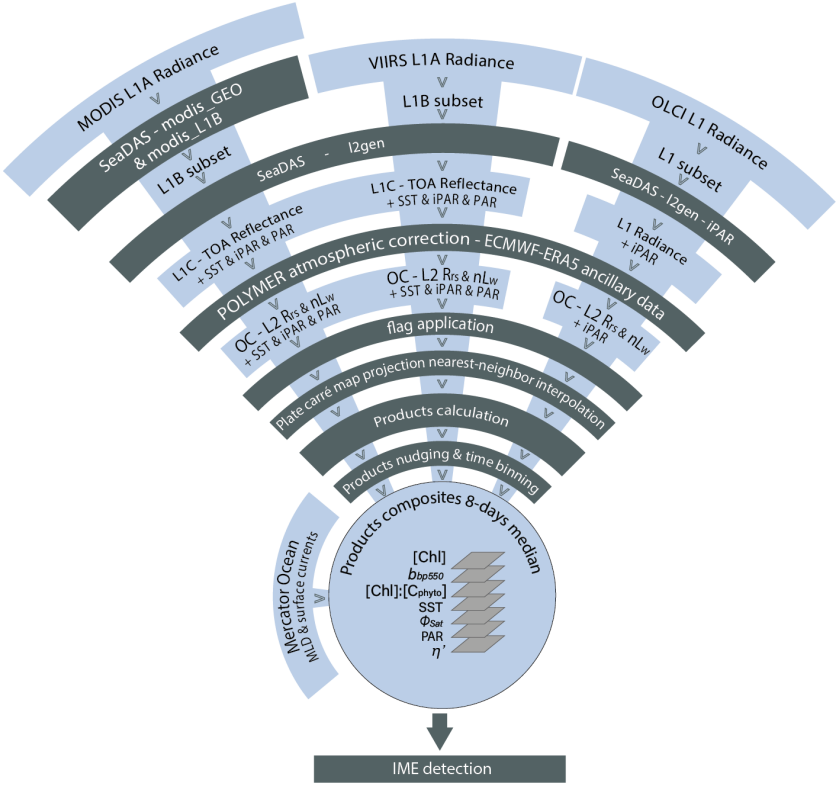

Figure A1. Satellite composite production flowchart.

A1 Satellite intermediate products computation

We derived the normalize leaving water radiance spectra (nL_w) from POLYMER normalized water reflectance spectra (R_w):

$$nL_w(\lambda) = R_w(\lambda) \times \frac{F_0}{\pi} \tag{A1}$$

where F_0 is the extraterrestrial solar flux at the time of observation:

$$F_0 = F_{0_{mean}}(\lambda) \times \left(\frac{d}{d_{mean}}\right)^2 \tag{A2}$$

where $F_{0_{mean}}(\lambda)$ is the solar spectral irradiance in $W/m^2/\mu m$ based on Thuillier et al. (2003) and spectrally weighted to each sensor's band spectral response, and where $\left(\frac{d}{d_{mean}}\right)^2$ is the normalized Sun-Earth distance at the time of observation (Whiteman and Allwine, 1986).

The normalized fluorescence line height ($nFLH$) was calculated from nL_w as in Behrenfeld et al. (2009):

$$nFLH = nL_w(678) - (\frac{70}{81}) \times nL_w(667) - (\frac{11}{81}) \times nL_w(748) \tag{A3}$$

https://doi.org/10.5194/egusphere-2025-4261
Preprint. Discussion started: 20 October 2025

We estimated SST from MODIS-Aqua and Terra, and VIIRS-SNPP L1A scenes using SeaDAS l2gen and only keeping high-quality pixels (i.e. 0 and 1 SST quality scores).

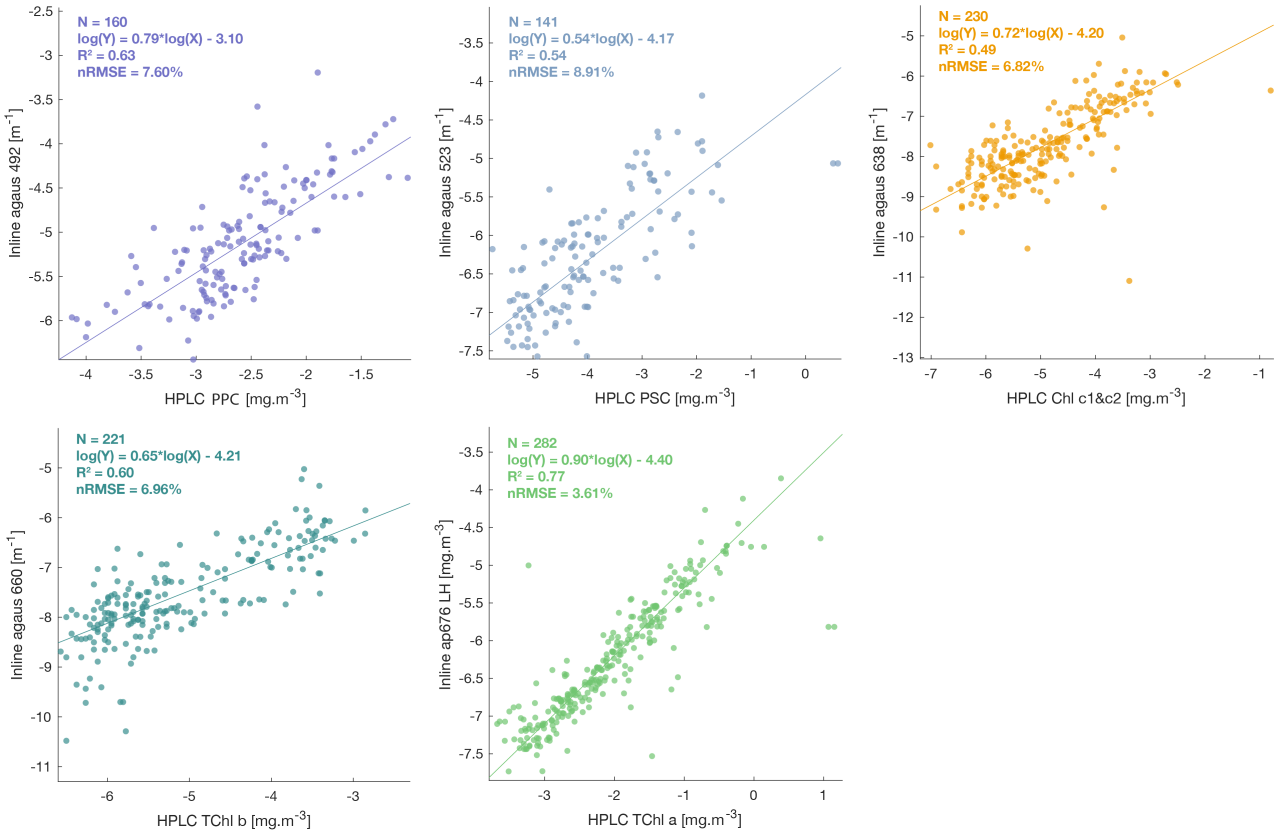

Figure A2. Robust linear regressions between phytoplankton pigments measured from HPLC and optical proxies for phytoplankton pigments estimated from a_p spectra (Chase et al., 2013) from the underway system (in log/log scale) during the *Tara* Pacific expedition (May 2016 to October 2018).

A2 in situ to satellite Match-ups

Match-ups between the calibrated in situ data collected from the underway system were performed following recommendations from Bailey and Werdell (2006). Underway data falling within ± 3 hours of each satellite overpass were extracted and averaged. We extracted and averaged underway measurements within a ± 3-hour period of each satellite overpass (i.e. Aqua and SNPP 13:30, Terra 10:30, Sentinel 3a and 3b 10:00, JPSS1 14:20 local time at the equator) and satellite data from the 25 closest pixels to underway data locations. We computed the median coefficient of variation (CV) of nL_w for bands between 412 and 555 nm and for the aerosol optical thickness at 865 nm. We tested several homogeneity thresholds and minimum unmasked number of pixels for each parameter matched to maximize the number of valid match-ups without introducing noise to the in situ-satellite

https://doi.org/10.5194/egusphere-2025-4261
Preprint. Discussion started: 20 October 2025

correlations. We kept only [Chla] match-ups with a minimum of 7 unmasked pixels and CV lower than 0.15 (see Appendix B in Bourdin et al., 2025). We kept iPAR match-ups with a minimum of 5 unmasked pixels and CV lower than 0.7 (Fig. A3). The SST quality score being already very restrictive, we kept match-ups with at least one unmasked pixel (i.e. SST-quality 0 and 1; Fig. A3).

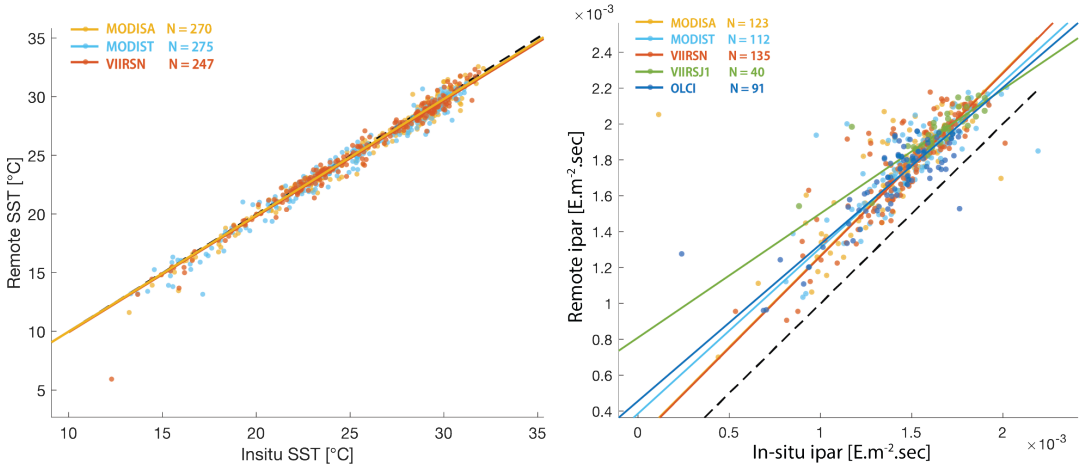

Figure A3. Robust linear regressions between in situ and satellite SST and iPAR. The in situ data were measured during the *Tara* Pacific expedition (May 2016 to October 2018).

Table A1. Robust correlations parameters of match-ups between satellite and in situ underway data

Variables	Satellite sensor	R^2	nRMSE [%]	Slope	Intercept	N
[Chl a]	MODISA	0.78	24.38	1.09	-0.01	111
	MODIST	0.81	20.48	1.08	-0.01	96
	VIIRSN	0.82	16.18	0.90	-0.19	109
	VIIRSJ1	0.70	31.47	1.02	0.05	27
	OLCI	0.79	16.56	0.89	-0.13	85
SST	MODISA	0.98	2.04	0.987	0.11	270
	MODIST	0.98	2.18	0.988	0.03	275
	VIIRSN	0.98	1.87	0.99	0.07	247
iPAR	MODISA	0.51	4.62	1.02	$2.5e^{-4}$	123
	MODIST	0.68	5.22	0.94	$3.6e^{-4}$	117
	VIIRSN	0.81	5.03	1.11	$9.9e^{-5}$	104
	VIIRSJ1	0.67	3.05	0.66	$8.6e^{-4}$	33
	OLCI	0.76	6.35	0.88	$4.5e^{-4}$	78

https://doi.org/10.5194/egusphere-2025-4261
Preprint. Discussion started: 20 October 2025

A3 MODIS b_{bp} artifacts

b_{bp} estimated from MODIS POLYMER R_{rs} (Fig. A4.2.a and 2.b) showed inverse spatial patterns compared to [Chla] computed from all sensors (Fig. A4.3) and also b_{bp} estimated from OLCI and VIIRSN R_{rs} (Fig. A4.2.c and 2.d) in ultra-oligotrophic regions ($[Chla] < 0.04\ mg\ m^{-3}$). These inverse spatial patterns were not observed with b_{bp} computed from SeaDAS R_{rs} (Fig. A4.1.a, 1.b, 1.c, and 1.d). The atmospheric correction of SeaDAS (i.e. l2gen) does not correct for the adjacency effect, while POLYMER does (i.e. the last term of the polynomial fit used to model the atmospheric reflectance accounts for the adjacency effect). The b_{bp} values in ultra-oligotrophic regions were largely within the range of noise added by the adjacency effect around clouds. Subsequently, the 8-day median b_{bp} products computed from SeaDAS R_{rs} for each satellite were so noisy that most of the signal due to the b_{bp} artifact in ultra-oligotrophic regions was masked by the adjacency effect. Therefore, only b_{bp} from VIIRSN and OLCI were binned into the 8-day median and used in further analysis.

A4 Uncertainty estimates

The 8-day merged satellite product composites were derived as described for [Chl] in Bourdin et al. (2025), using multiple overpasses and sensors. For the 2500-km^2 region around the Fiji archipelago, composites typically include 120 daytime ocean color scenes and 240 SST scenes (daytime and nighttime). Each pixel of the merged products is a median of the n number of observations of the original images, with standard deviations (σ_{bin}) representing the temporal variability for a given pixel during each 8-day period and the variability between sensors (after nudging, when applied). We computed Φ_{Sat} only from the MODIS and OLCI sensors due to a missing band in VIIRS for the computation of $nFLH$. Binned b_{bp} were only obtained from OLCI and VIIRS sensors due to an artifact in the MODIS estimates of this variable (Appendix A3). Therefore, the number of observations in the binned Φ_{Sat} and b_{bp} was reduced, resulting in noisier maps.

We propagated known uncertainties from in situ data to satellite merged end-products following the same strategy as in Bourdin et al. (2025). We estimated the error associated with the computation of bio-optical proxies from in situ continuous underway data, using the normalized root mean square error ($nRMSE_{udw}$ in %) of the correlation between the underway estimates and their corresponding calibrated measurement when available (e.g. total [Chla] from HPLC correlated with [Chla] line-height in Bourdin et al. (2025)). Similarly, we estimated the error associated with bio-optical proxies computation from satellite data using the $nRMSE_{sat}$ of the relation between each satellite estimate and its calibrated underway counterpart when available (e.g. [Chla] see Appendix B in Bourdin et al. (2025) and SST and iPAR in Fig. A3 and Table A1). Since no measurements of C_{phyto} were performed in situ, we propagated to the binned C_{phyto} the uncertainty estimates of the published empirical relationships we used between b_{bp} and C_{phyto} (32%; Graff et al., 2015)). Unfortunately, the relation between in situ b_{bp} and satellite b_{bp} was very sensitive to match-up criteria and the linear regressions were not well constrained, potentially due to low quality of in situ data (due to bio-fouling or bubbles in the underway line) or due to large uncertainty in satellite retrieval (Bisson et al., 2021). Therefore, b_{bp}, like all the other variables for which no calibrated in situ data were available, was nudged to best match a reference satellite sensor (see 2.5). In these cases, the error associated with the nudging process (i.e. $nRMSE_{sat}$ of the regressions) was propagated to the binned products' uncertainty estimates. In all of these cases, the

https://doi.org/10.5194/egusphere-2025-4261
Preprint. Discussion started: 20 October 2025

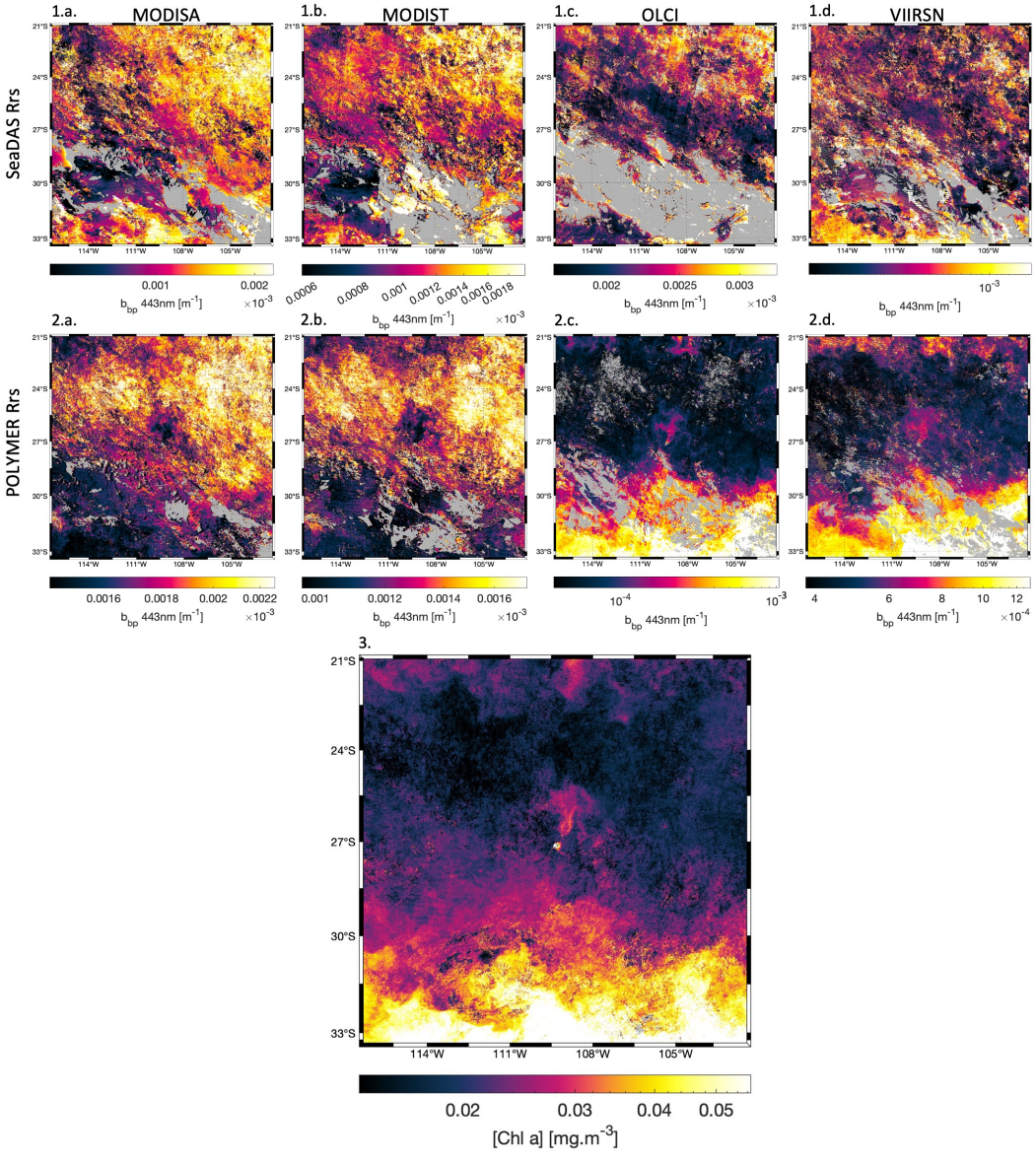

Figure A4. Comparison of 8-day medians (11 to 18 October 2016) of b_{bp} around Rapa Nui for (a) MODISA, (b) MODIST, (c) OLCI, and (d) VIIRSN, using the atmospheric corrections (1) SeaDAS R_{rs} (top row), (2) POLYMER R_{rs} (middle row), and (3) the corresponding 8-day median of [Chla] computed using POLYMER R_{rs} of all satellites.

uncertainties of the binned satellite end-products were computed as follows:

$$\sigma_V = \sqrt{\sigma^2_{Vbin} + \sum_{n=1}^{n_c} (\tilde{V} * nRMSE_c)^2} \tag{A4}$$

https://doi.org/10.5194/egusphere-2025-4261
Preprint. Discussion started: 20 October 2025

with $\tilde{V}$ the binned variable, n_c the number of calibration/correction, and $nRMSE_c$ the $nRMSE$ associated with each of the n_c corrections. The uncertainty associated with the correction of each variable was saved in the data files (Bourdin, 2025). When no good relationship with in situ data or reference satellite data was found, 'NaN' values are saved in the $nRMSE$ columns of the data files. In these cases, the final σ_V of a given 8-day median pixel only represents the natural variability over the 8-day period and the variability between sensors. The standard error of the mean of the adjusted satellite end-products of each pixel was computed as follows:

$$SEM_V = \frac{\sigma_V}{\sqrt{n_{V_{bin}}}} \tag{A5}$$

The final uncertainty estimate associated with the adjusted satellite binned variable (V) within the entire IME or BO zones ($SEM^f_{[V]_{IME}}$) as presented in Fig. E1, Fig. E2, Fig. E3, and Fig. 6 were expressed as the mean standard error of the mean of V within entire IME or BO zones:

$$SEM^f_{V_{IME}} = \frac{\overline{\sigma}_{V_{IME}}}{\sum n_{V_{bin_{IME}}}} + S_{V_{unc}} \times \overline{V}_{IME} \tag{A6}$$

with $\sum n_{V_{bin_{IME}}}$ the total number of V observations within the IME zone before merging, and $S_{V_{unc}}$ the weighted bias associated with the calculation of the slopes of the regressions between the calibrated in situ variable and each satellite estimate V. $S_{V_{unc}}$ was computed as follows:

$$S_{V_{unc}} = |1 - S_{V\,sat}| \times \frac{n_{M_{sat}}}{N_{M_{tot}}} \tag{A7}$$

with $S_{V\,sat}$ the slope of the relation between V of a given satellite and its in situ equivalent, $n_{M_{sat}}$ the number of valid match-ups of the same satellite, and $N_{M_{tot}}$ the total number of valid match-ups. $S_{V_{unc}}$ represents the maximum bias associated with the calculation of the merged satellite variable V, which we assume to be equivalent to the potential likelihood bias of the merged satellite variable V. Assuming sufficient valid matches with each satellite, $S_{V_{unc}}$ is a conservative estimate of the bias associated with the slope computation because the merging method forces each satellite V to agree with in situ data using sensor-specific corrections, which likely reduces the bias of the merged product. This method was applied to compute the uncertainty of all satellite merged variables except η', the IME surface area, and the surface-area integrated [Chla] ($\sum[Chla]_{IME}$). IME area uncertainties ($\sigma_{A_{IME}}$) were computed during the detection of the IME [Chla] contours as the difference in the IME area between the last two iterations of the [Chla] contours:

$$\sigma_{A_{IME}} = A_{IME_{cChl_f}} - A_{IME_{cChl_{f-1}}} \tag{A8}$$

with $A_{IME_{cChl_f}}$ the IME area at the final IME contour value and $A_{IME_{cChl_{f-1}}}$ the IME area at the previous contour value. Therefore, $\sigma_{A_{IME}}$ represents the area detection resolution associated with the size of the step of [Chla] iteration. The uncertainties associated with the estimation of IME surface-area integrated [Chla] ($\sum[Chla]_{IME}$) were computed as follows:

$$SEM^f_{\sum[Chla]_{IME}} = \sum[Chla]_{IME} \times \sqrt{\left(\frac{SEM^f_{[Chla]_{IME}}}{\overline{[Chla]}_{IME}}\right)^2 + \left(\frac{\sigma_{A_{IME}}}{A_{IME}}\right)^2} \tag{A9}$$

https://doi.org/10.5194/egusphere-2025-4261
Preprint. Discussion started: 20 October 2025

We estimated uncertainties in η'_{obs} (i.e. $[Chla]/[C_{phyto}]$) as:

$$SEM_{\eta'_{obs}} = \eta'_{obs} \times \sqrt{\left(\frac{SEM_{[Chla]}}{[Chla]}\right)^2 + \left(\frac{SEM_{[C_{phyto}]}}{[C_{phyto}]}\right)^2} \tag{A10}$$

Similarly:

$$SEM_{I_{ML}} = I_{ML} \times \sqrt{\left(\frac{SEM_{PAR}}{PAR}\right)^2 + \left(\frac{SEM_{MLD}}{MLD}\right)^2 + \left(\frac{SEM_{Kd_{PAR}}}{Kd_{PAR}}\right)^2} \tag{A11}$$

where SEM_{PAR} is the standard error of the mean of the merged daily PAR product, $SEM_{MLD} = max(0.2 \times MLD, 5\text{m})$, and $SEM_{Kd_{PAR}} = SEM_{[Chla]}$ since Kd_{PAR} is estimated from the [Chla] merged products.

Since η' ranges from negative to positive values, we expressed its uncertainties as follows:

$$SEM_{\eta'} = |\eta'| \times \sqrt{\left(\frac{SEM_{I_{ML}}}{I_{ML}}\right)^2 + \left(\frac{SEM_{\eta'_{obs}}}{\eta'_{obs}}\right)^2} \tag{A12}$$

We assumed that the uncertainties associated with the computation of $\hat{\eta}_{obs_{min}}$ and $\hat{\eta}_{obs_{max}}$ fits were negligible compared to $SEM_{I_{ML}}$ and $SEM_{\eta'_{obs}}$, given the substantial number of valid η'_{obs} pixels per I_{ML} bin used to compute $\hat{\eta}_{obs_{min}}$ and $\hat{\eta}_{obs_{max}}$ fits (on average 1.13×10^7 pixels per I_{ML} bin). Since the mixed layer is often shallower than Z_{eu} in this region, $Kd_{PAR_{Z_{eu}}} > Kd_{PAR_{MLD}}$. Therefore, we tested the sensitivity of η' computation using two different empirical methods to estimate Kd_{PAR} from [Chla]. In addition to the method presented in 2.4 for computing Kd_{PAR} from Z_{eu}, we estimate Kd_{490} from [Chla] and Kd_{PAR} from Kd_{490} using equations 8 and 9 from Morel et al. (2007). Differences in η' were negligible in all four case studies (that is, the maximum difference ranging from 10^{-3} to 0.05), and the spatial and temporal trends remained consistent between the two calculation methods.

Appendix B: Phytoplankton physiology in Rapa Nui, Society Islands, Samoa, and Fiji-Tonga' IMEs

We analyzed inbound and outbound transects around Rapa Nui, Society Islands, and Samoa to identify processes associated with potential nutrient enrichments, as done in section 3.2 for Fiji. In these three case studies, b_{bp} was not measured in situ, therefore, we computed the ratio between [Chla] and c_p660 ($[Chla]/c_p660$) as an alternative for $[Chla]/[C_{phyto}]$ (Fig. B1, B3, B5 Behrenfeld and Boss, 2006). These results show that $[Chla]/c_p660$, measured in situ along the transects, generally follows similar spatial trends to $[Chla]/[C_{phyto}]$ measured from satellite data, although the magnitude of these two ratios differs significantly. In all three cases, sudden synchronized changes in SST and SSS were detected along the inbound and outbound transects, indicating the presence of fronts between different water masses. These water mass changes were accompanied by higher $[Chla]/c_p660$ in the IME zone on the outbound transects of Rapa Nui (Fig. B1) and the Society Islands (also associated with lower $[PPC]/[Chla]$ in that case; Fig. B3), suggesting the upwelling of low-light-adapted cells to the surface. No evidence of such upwelling was detected around Samoa; however, the strong increase in SST and decrease in SSS detected while crossing the IME zone south of Samoa on the inbound transect indicate a front between BO waters and IME waters. The IME zone properties were similar to those of coastal water masses characterized by significantly high nitrogen concentrations

https://doi.org/10.5194/egusphere-2025-4261
Preprint. Discussion started: 20 October 2025

for the region (up to 1 μM of dissolved organic nitrogen), higher SST, and lower, more variable SSS, which are typical of water masses influenced by freshwater discharge (Fig. B5). These findings suggest that the IME zone observed offshore along the inbound transect was likely caused by nitrogen inputs from terrigenous sources, discharged into the coastal ocean via rivers, and subsequently advected offshore by coastal currents. Figure B4 reveals an artificially sharp line of increasing Φ_{Sat} across the outbound transect, likely due to an anomaly in $nFLH$ or iPAR estimation. To avoid misinterpretation, this section was removed from Figure B3 on the outbound transect. Overall, Φ_{Sat} consistently decreased when approaching each of these three islands, and was generally associated with increased total iron concentration, although two stations exhibited low total iron concentrations close to shore, notably on the inbound transects of Rapa Nui and Samoa. In contrast, the decrease in η' near these three islands was more variable. While η' declined in Samoa's IME, it only exhibited a marginal decrease in the IME zones of Rapa Nui and the Society Islands, despite signatures of upwelling being detected during these transects. In all cases, η' decreased sharply in the coastal zones, where the 8 km spatial resolution of the MLD product used for computing η' is likely too coarse to accurately estimate I_{ML} and η'.

https://doi.org/10.5194/egusphere-2025-4261
Preprint. Discussion started: 20 October 2025

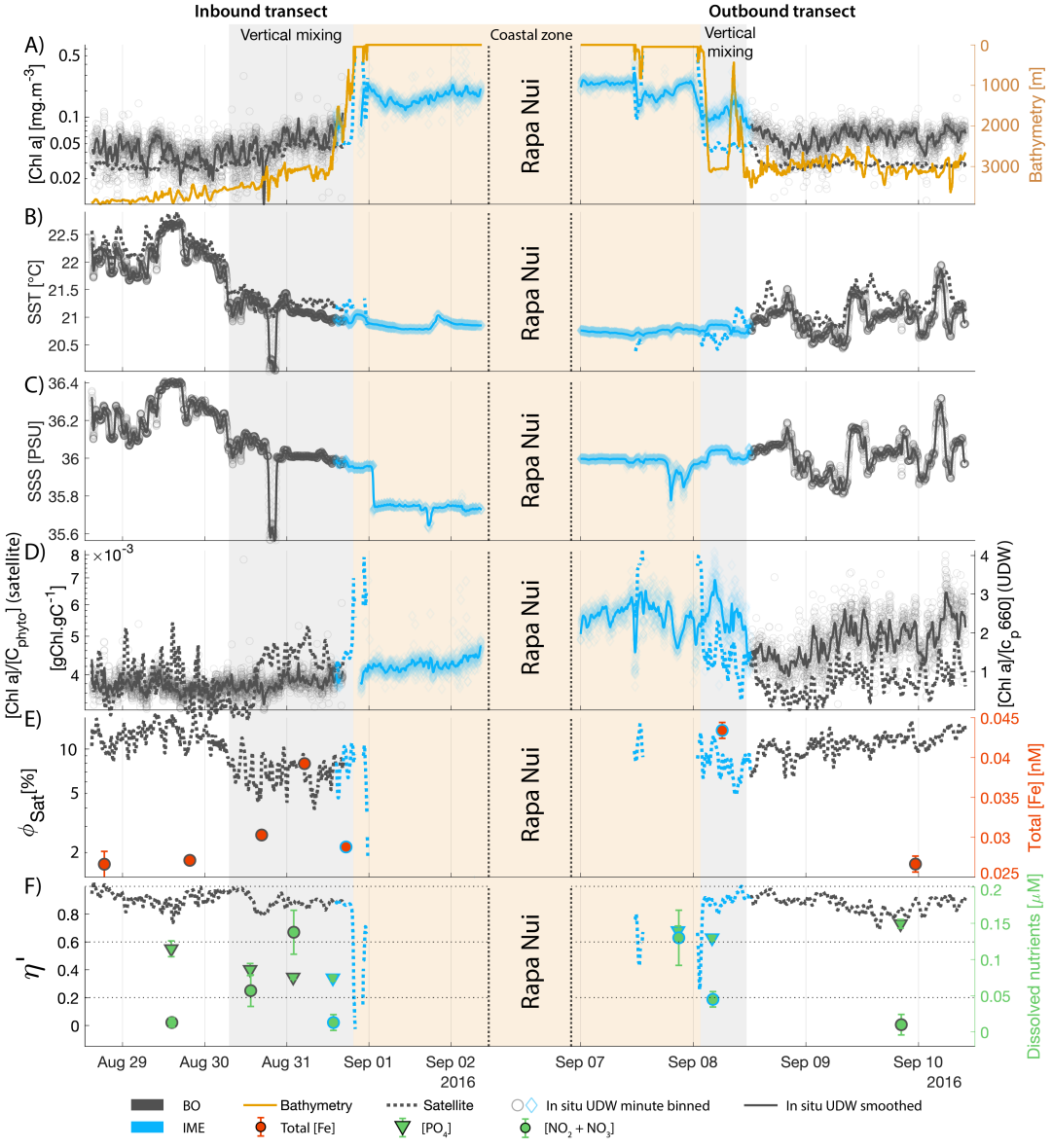

Figure B1. Underway data measured during the inbound (left panels) and outbound (right panels) transects around Rapa Nui and their satellite counterparts, when available. **A)** Chlorophyll a concentration ([Chla]) and bathymetry, **B)** sea surface temperature (SST), **C)** sea surface salinity (SSS), **D)** [Chla] to phytoplankton carbon ratio from satellite ($[Chla]/[C_{phyto}]$) and [Chla] to beam attenuation at 660 nm from in-situ underway ($[Chla]/c_p660$), **E)** fluorescence quantum yield (Φ_{Sat}; iron stress index) and total iron concentration measured at sampling stations, **F)** macronutrient stress index (η') and macronutrient concentrations measured at sampling stations. The blue points show in situ data falling in IME zones detected on the overlapping 8-day satellite composite (BO = black circle, IME = blue diamond). The points show the minute-binned underway data, and the solid lines represent the underway data smoothed with a 2h low-pass digital filter. The gray shaded area highlights the coastal upwelling zone, and the beige shaded area highlights the transect over shallow waters (< 100 m depth).

https://doi.org/10.5194/egusphere-2025-4261
Preprint. Discussion started: 20 October 2025

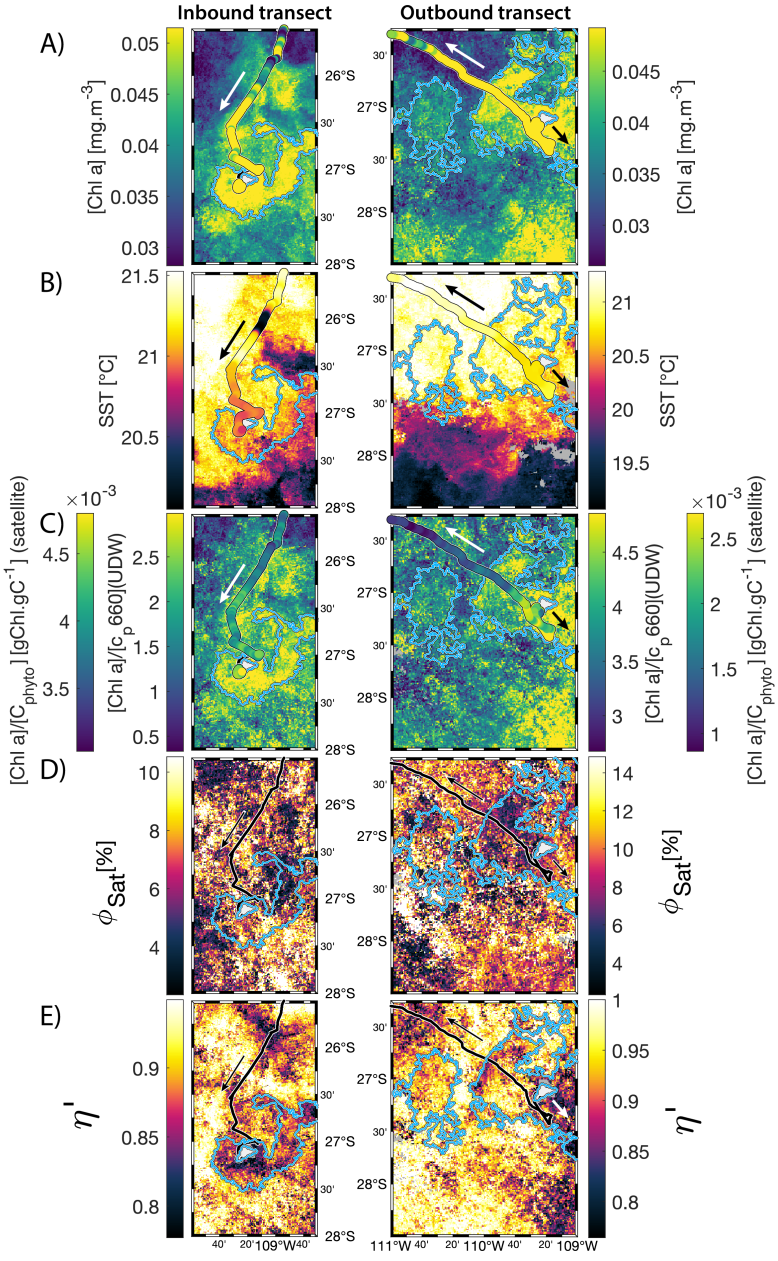

Figure B2. 8-day median satellite maps zoomed on the inbound (left-hand-side panels) and outbound transects (right-hand-side panels) around Rapa Nui (arrow shows sailing direction). The blue contour delineates the island mass effect zone detected from satellite chlorophyll *a* concentration ([Chla]). In situ underway measurements are overlaid on the satellite map if the same variable was measured from satellite estimates and the underway system. **A)** [Chla], **B)** sea surface temperature (SST), **C)** [Chla] to phytoplankton carbon ratio from satellite ($[Chla]/[C_{phyto}]$) and [Chla] to beam attenuation at 660 nm from in-situ underway ($[Chla]/c_p660$), **D)** fluorescence quantum yield (ϕ_{Sat}), **E)** macronutrient stress index (η').

https://doi.org/10.5194/egusphere-2025-4261
Preprint. Discussion started: 20 October 2025

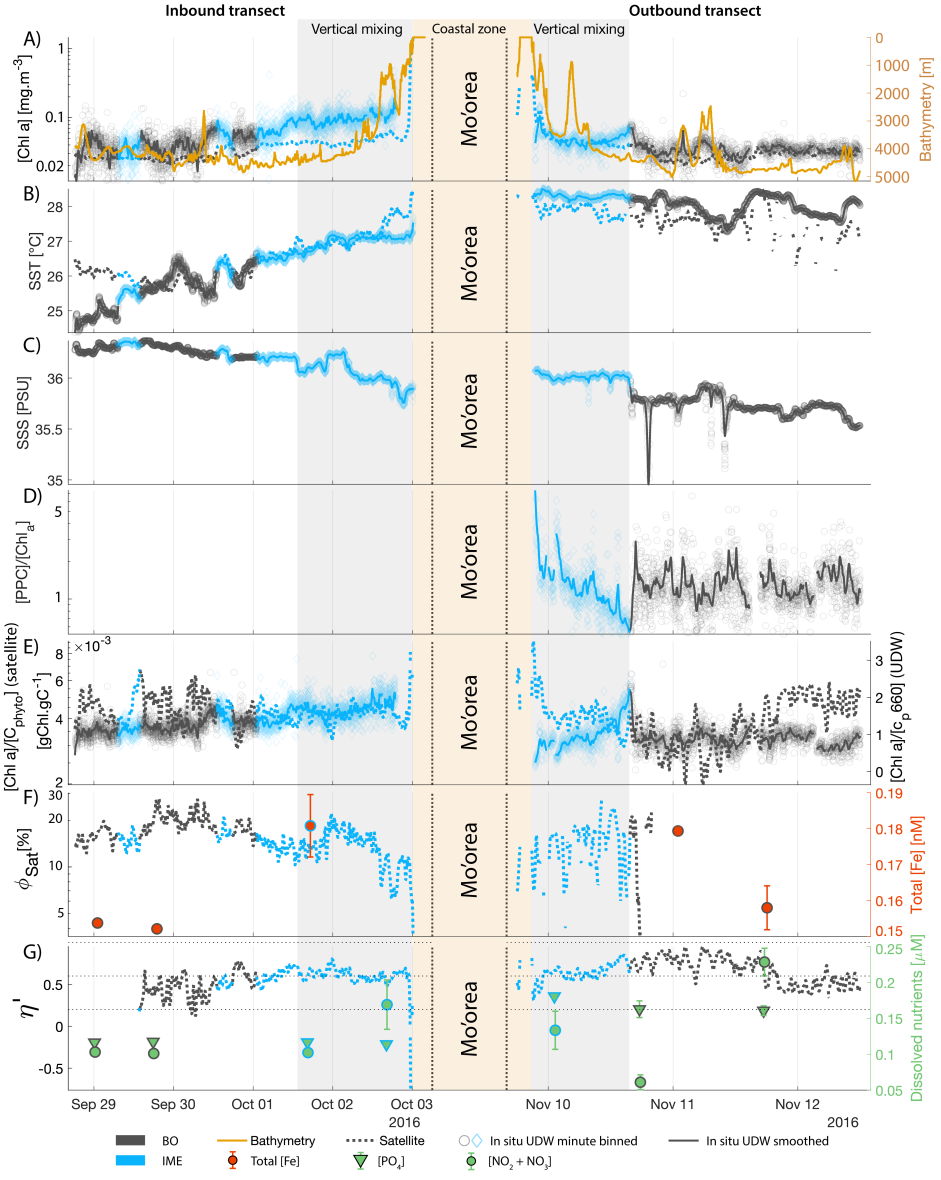

Figure B3. Underway data measured during the inbound (left panels) and outbound (right panels) transects around Society Islands and their satellite counterparts, when available. **A)** Chlorophyll a concentration ([Chla]) and bathymetry, **B)** sea surface temperature (SST), **C)** sea surface salinity (SSS), **D)** Photo-protective carotenoids proportion ($[PPC]/[Chla]$), **E)** [Chla] to phytoplankton carbon ratio from satellite ($[Chla]/[C_{phyto}]$) and [Chla] to beam attenuation at 660 nm from in-situ underway ($[Chla]/c_p660$), **F)** fluorescence quantum yield (Φ_{Sat}; iron stress index) and total iron concentration measured at sampling stations, **G)** macronutrient stress index (η') and macronutrient concentrations measured at sampling stations. The blue points show in situ data falling in IME zones detected on the overlapping 8-day satellite composite (BO = black circle, IME = blue diamond). The points show the minute-binned underway data, and the solid lines represent the underway data smoothed with a 2h low-pass digital filter. The gray shaded area highlights the coastal upwelling zone, and the beige shaded area highlights the transect over shallow waters (< 100 m depth).

https://doi.org/10.5194/egusphere-2025-4261
Preprint. Discussion started: 20 October 2025

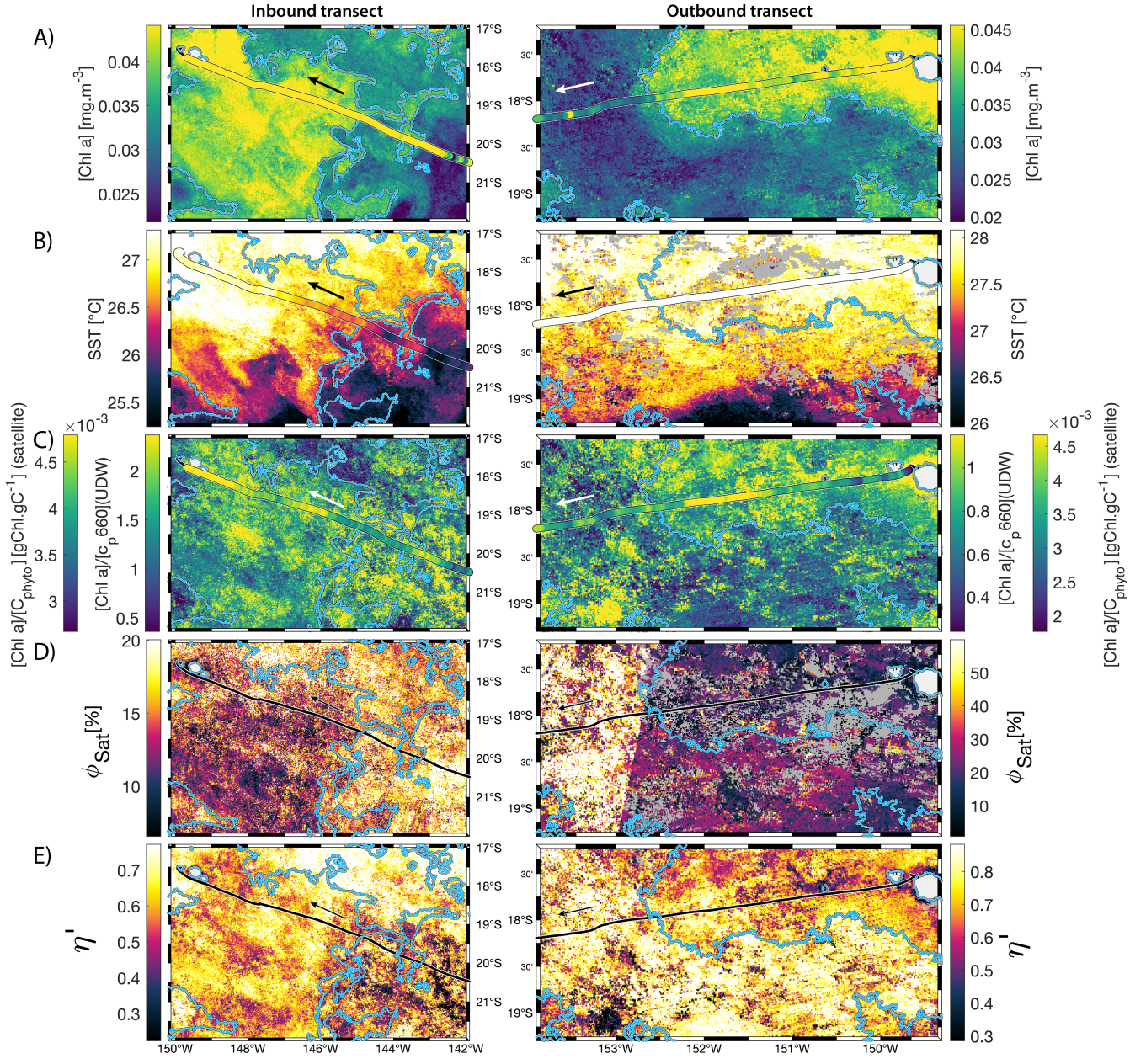

Figure B4. 8-day median satellite maps zoomed on the inbound (left-hand-side panels) and outbound transects (right-hand-side panels) around Society Islands (arrow shows sailing direction). The blue contour delineates the island mass effect zone detected from satellite chlorophyll *a* concentration ([Chla]). In situ underway measurements are overlaid on the satellite map if the same variable was measured from satellite estimates and the underway system. **A)** [Chla], **B)** sea surface temperature (SST), **C)** [Chla] to phytoplankton carbon ratio from satellite ($[Chla]/[C_{phyto}]$) and [Chla] to beam attenuation at 660 nm from in-situ underway ($[Chla]/c_p660$), **D)** fluorescence quantum yield (ϕ_{Sat}), **E)** macronutrient stress index (η').

https://doi.org/10.5194/egusphere-2025-4261
Preprint. Discussion started: 20 October 2025

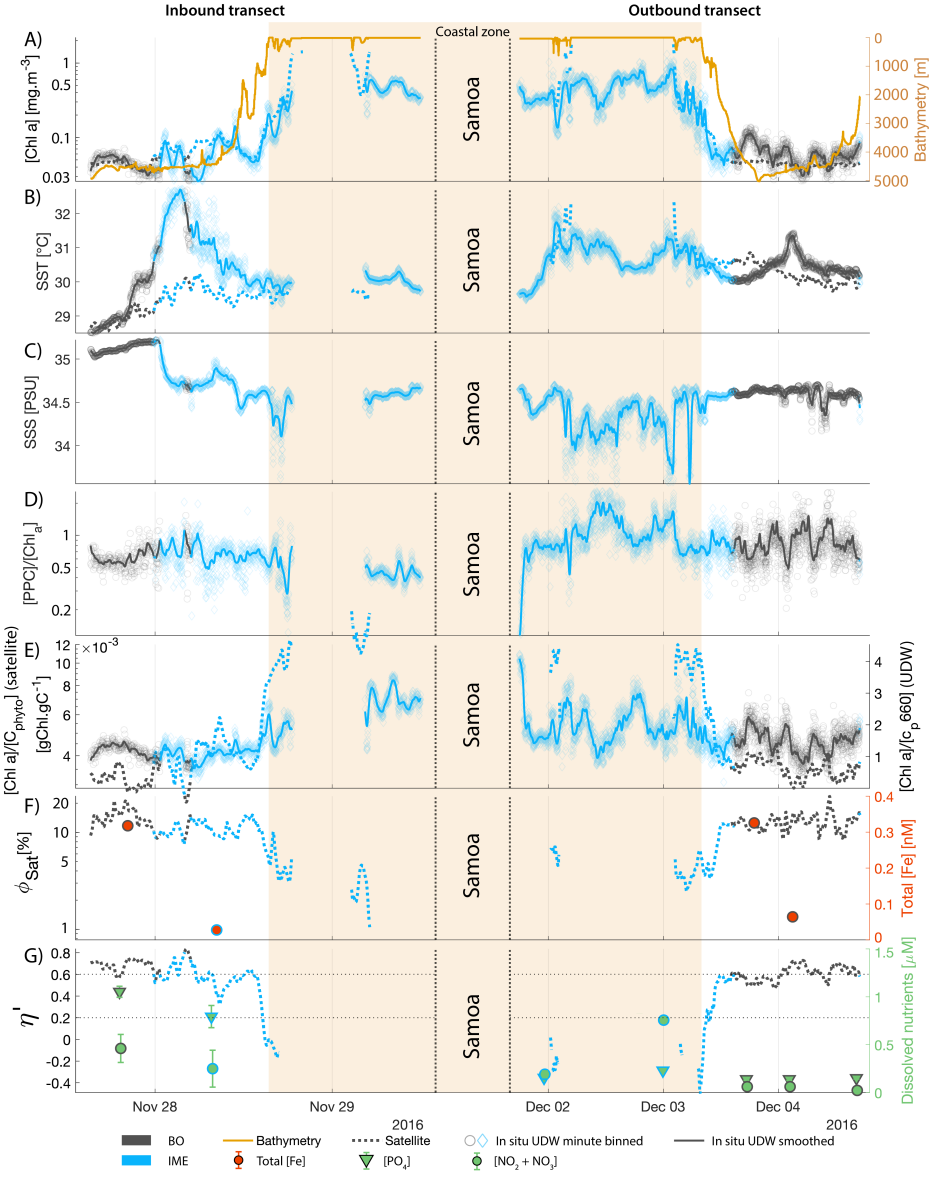

Figure B5. Underway data measured during the inbound (left panels) and outbound (right panels) transects around Samoa and their satellite counterparts, when available. **A)** Chlorophyll a concentration ([Chla]) and bathymetry, **B)** sea surface temperature (SST), **C)** sea surface salinity (SSS), **D)** Photo-protective carotenoids proportion ($[PPC]/[Chla]$), **E)** [Chla] to phytoplankton carbon ratio from satellite ($[Chla]/[C_{phyto}]$) and [Chla] to beam attenuation at 660 nm from in-situ underway ($[Chla]/c_p660$), **F)** fluorescence quantum yield (Φ_{Sat}; iron stress index) and total iron concentration measured at sampling stations, **G)** macronutrient stress index (η') and macronutrient concentrations measured at sampling stations. The blue points show in situ data falling in IME zones detected on the overlapping 8-day satellite composite (BO = black circle, IME = blue diamond). The points show the minute-binned underway data, and the solid lines represent the underway data smoothed with a 2h low-pass digital filter. The gray shaded area highlights the coastal upwelling zone, and the beige shaded area highlights the transect over shallow waters (< 100 m depth).

https://doi.org/10.5194/egusphere-2025-4261
Preprint. Discussion started: 20 October 2025

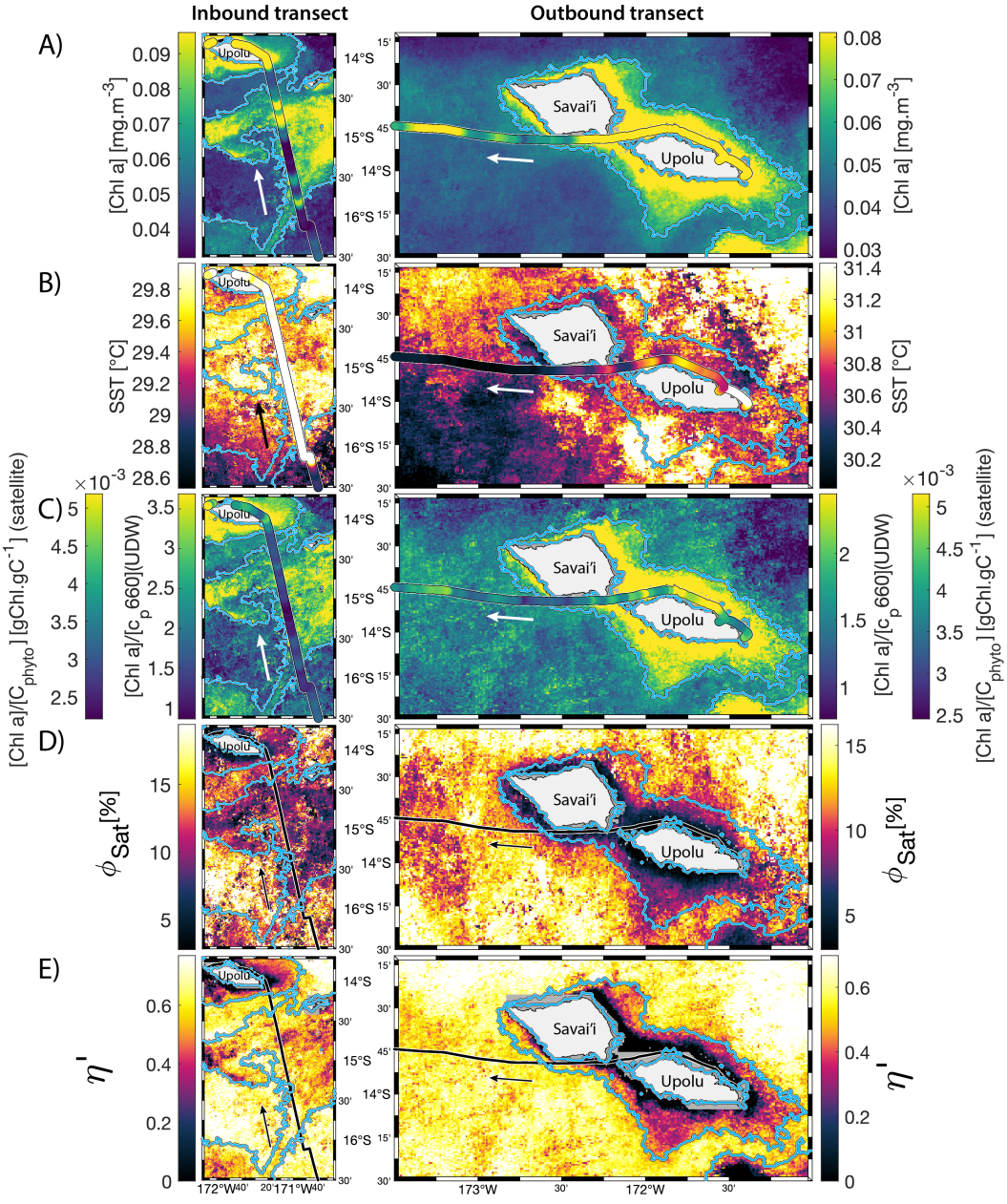

Figure B6. 8-day median satellite maps zoomed on the inbound (left-hand-side panels) and outbound transects (right-hand-side panels) around Samoa (arrow shows sailing direction). The blue contour delineates the island mass effect zone detected from satellite chlorophyll *a* concentration ([Chla]). In situ underway measurements are overlaid on the satellite map if the same variable was measured from satellite estimates and the underway system. **A)** [Chla], **B)** sea surface temperature (SST), **C)** [Chla] to phytoplankton carbon ratio from satellite ($[Chla]/[C_{phyto}]$) and [Chla] to beam attenuation at 660 nm from in-situ underway ($[Chla]/c_p660$), **D)** fluorescence quantum yield (ϕ_{Sat}), **E)** macronutrient stress index (η').

https://doi.org/10.5194/egusphere-2025-4261
Preprint. Discussion started: 20 October 2025

We classified the continuous underway data into three different categories to identify the differences in the studied variables between the background ocean (BO), coastal IME, and advected IME. Underway data located outside IME zones that were delineated from satellite data, and with a bathymetry deeper than 100 m, were included in the BO category. Underway data located inside the IME zones detected from satellite data and with a bathymetry deeper than 100 m were included in the 'IME advected' category, and underway data located inside the IME zones but from locations with a bathymetry shallower than 100 m were grouped into the 'IME coastal' category. We extracted different parameters, all measured from the underway continuous system, and tested if they were significantly different between categories. First, we tested the data normality of each category separately using a Lilliefors test. If all categories passed the normality test, we used a parametric analysis of variance (ANOVA) to test for significant differences between categories. If one or more categories failed the normality test, we used a non-parametric Kruskal-Wallis test.

These categories include data measured during both the inbound and outbound transect for each of the four island groups analyzed with different duration separating the inbound and outbound transects for stopover (i.e. 7 days for Rapa Nui, 38 days for Mo'orea in the Society Islands, 5 days for Samoa, and 10 days for Fiji; see Fig. 3, Fig. B1, Fig. B3, Fig. B5). Therefore, the comparison of in situ bio-optical properties between the three categories highlights differences consistent over the inbound and outbound transects (Fig. B7 and Fig. D1). However, it is important to acknowledge that different water masses were sampled between these transects, particularly in the case of the Society Islands, where 38 days separated the inbound and outbound transects.

https://doi.org/10.5194/egusphere-2025-4261
Preprint. Discussion started: 20 October 2025

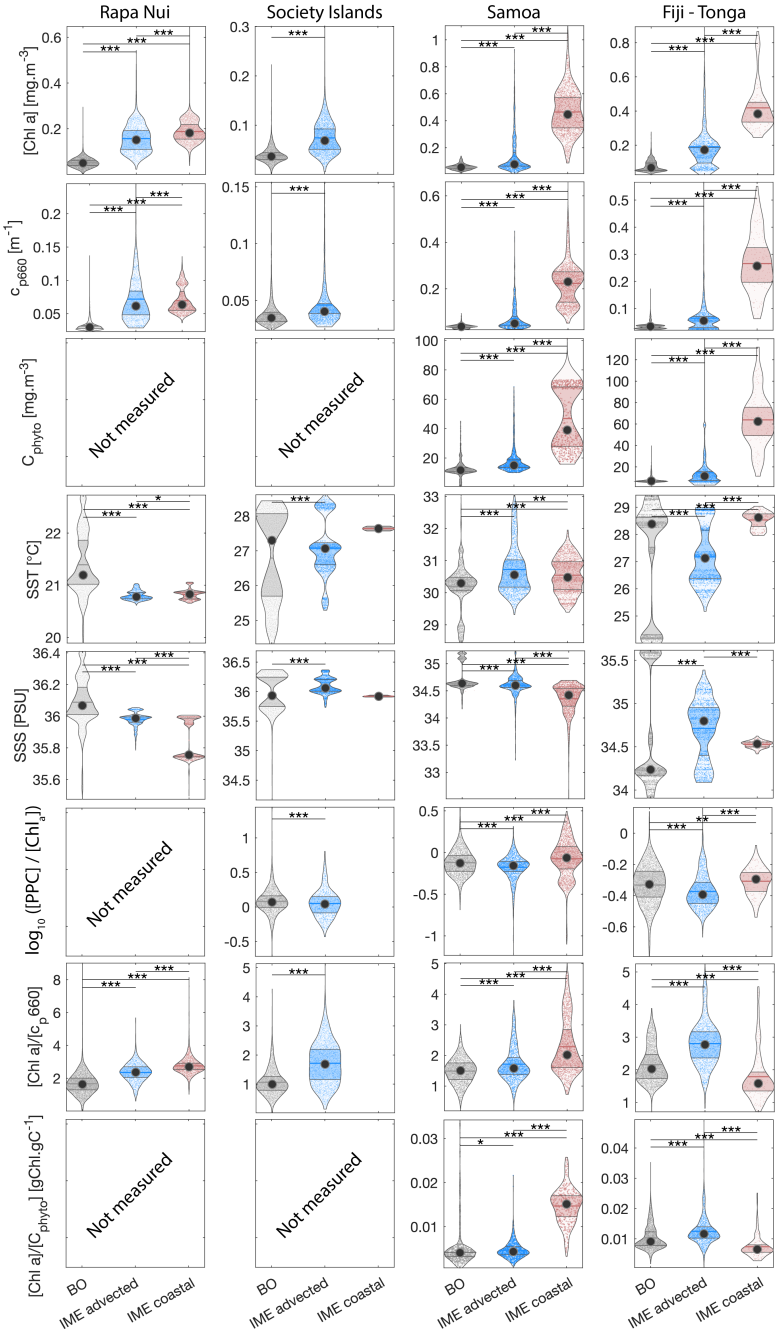

Figure B7. Violin plots of continuous underway data related to phytoplankton concentration and physiology located in the background ocean, advected IME, and coastal IME zones. The four columns represent data measured around the four case studies, and different parameters are organized by rows.

https://doi.org/10.5194/egusphere-2025-4261
Preprint. Discussion started: 20 October 2025

Appendix C: Macronutrient and iron concentration

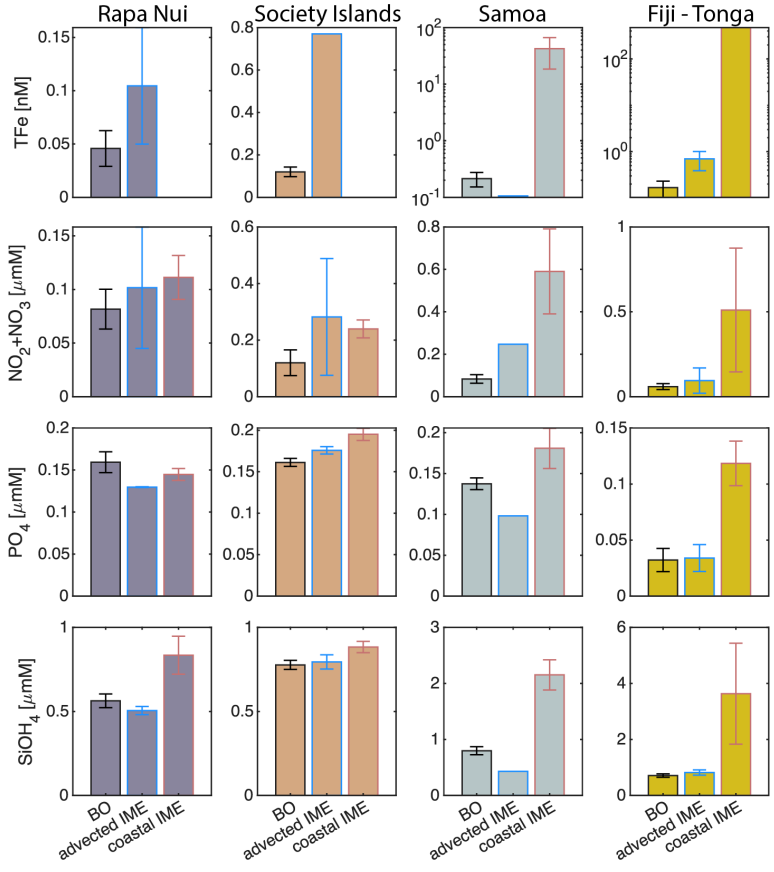

Figure C1. Macronutrient and iron concentrations at sampling stations located in the background ocean, advected IME, and coastal IME zones. The four columns represent data measured around the four case studies, and different parameters are organized by rows.

https://doi.org/10.5194/egusphere-2025-4261
Preprint. Discussion started: 20 October 2025

Appendix D: Phytoplankton community composition in Rapa Nui, Society Islands, Samoa, and Fiji-Tonga' IMEs

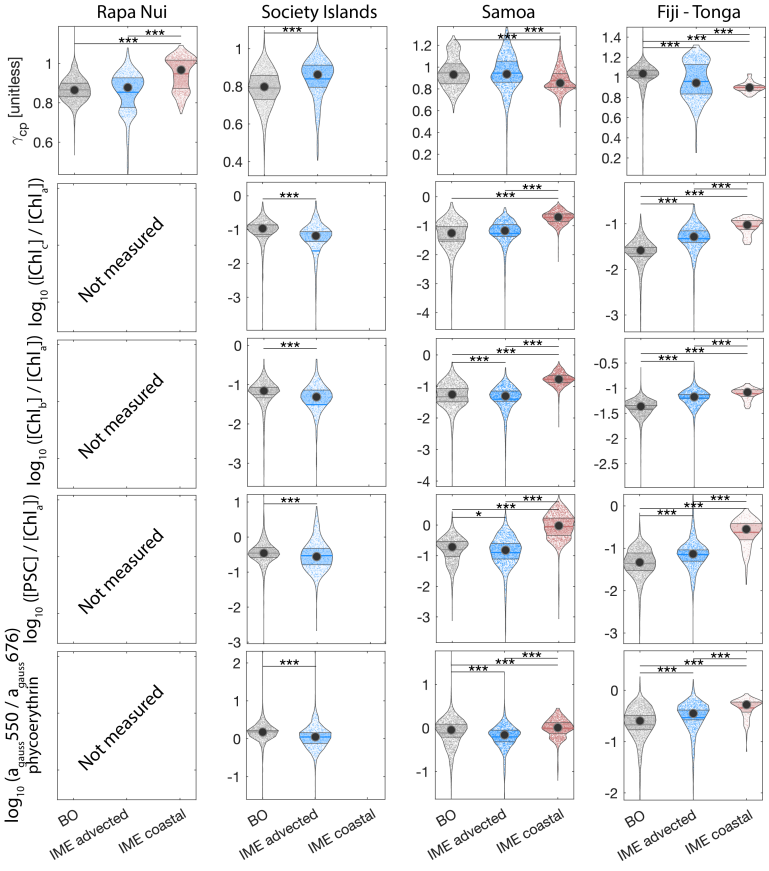

Figure D1. Violin plots of continuous underway data related to phytoplankton community composition located in the background ocean, advected IME, and coastal IME zones. The four columns represent data measured around the four case studies, and different parameters are organized by rows.

https://doi.org/10.5194/egusphere-2025-4261
Preprint. Discussion started: 20 October 2025

Appendix E: Temporal analysis of IME around Rapa Nui, Society Islands, and Samoa

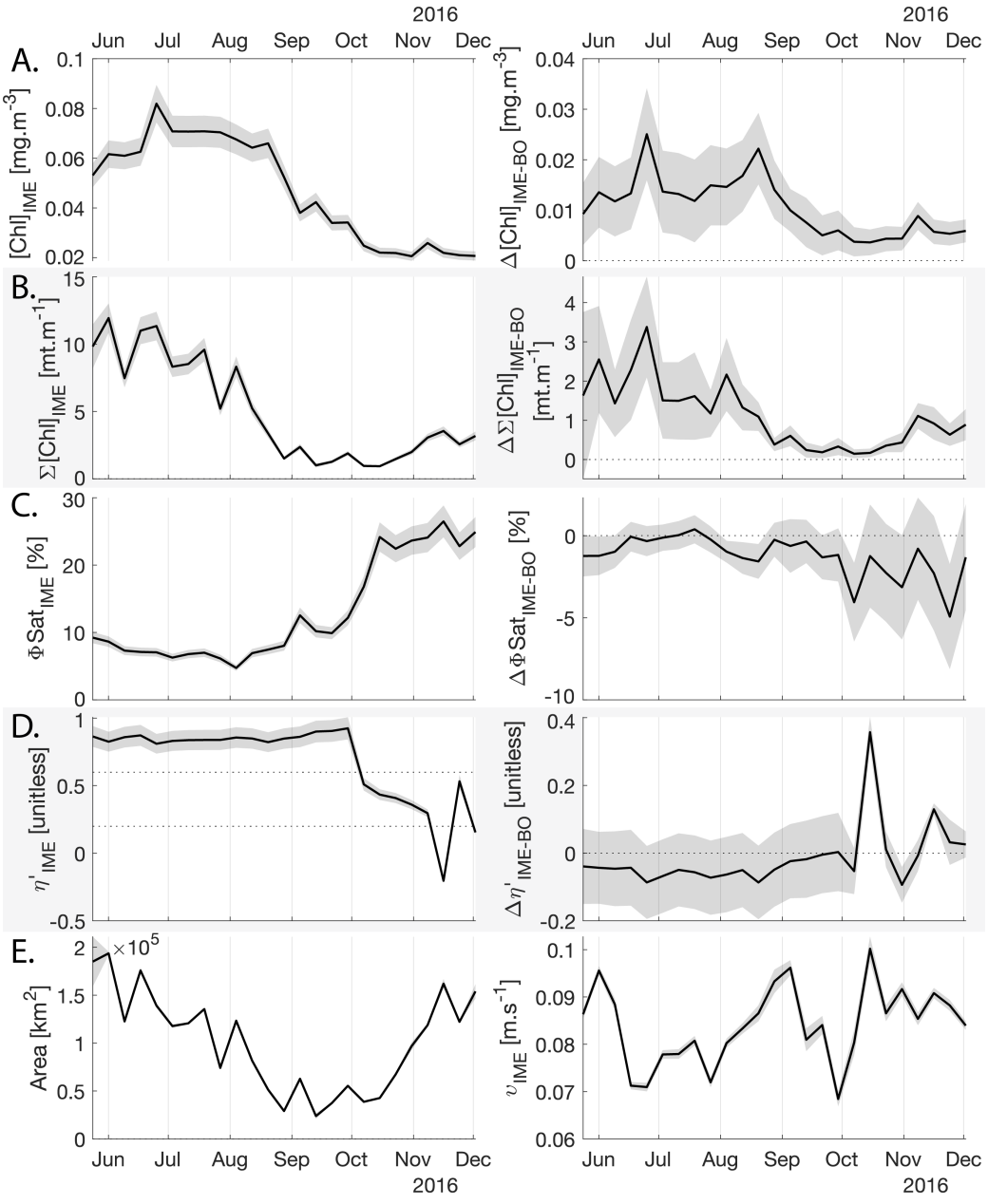

Figure E1. Six-month-long time series of satellite-derived IME properties of the IME zone detected around Rapa Nui. **A, B, C, and D left panels**: Average of properties within the IME zones, **A, B, C, and D right panels**: Difference between properties within the IME zones and the background ocean (BO). **A row**: chlorophyll *a* concentration ([Chla]), **B row**: IME integrated chlorophyll *a* ($\sum[Chla]_{IME}$), **C row**: fluorescence quantum yield (ϕ_{Sat}), **D row**: macronutrient stress index (η'), **E left:** IME zone area (in km^2), **E right**: surface current velocity.

https://doi.org/10.5194/egusphere-2025-4261
Preprint. Discussion started: 20 October 2025

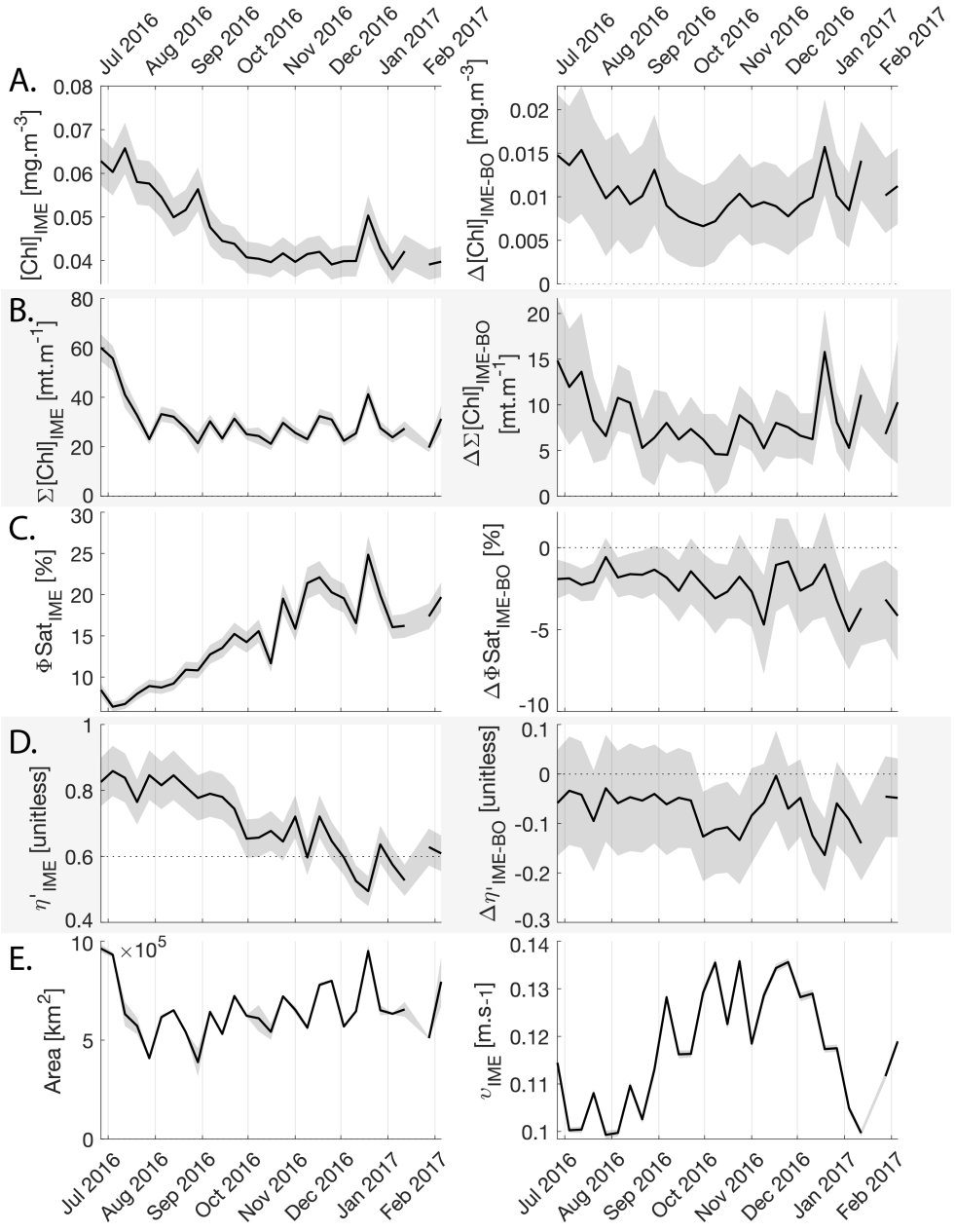

Figure E2. Six-month-long time series of satellite-derived IME properties of the IME zone detected around the Society Islands in French Polynesia. **A, B, C, and D left panels**: Average of properties within the IME zones, **A, B, C, and D right panels**: Difference between properties within the IME zones and the background ocean (BO). **A row**: chlorophyll *a* concentration ([Chla]), **B row**: IME integrated [Chla] ($\sum[Chla]_{IME}$), **C row**: fluorescence quantum yield (ϕ_{Sat}), **D row**: macronutrient stress index (η'), **E left:** IME zone area (in km^2), **E right**: surface current velocity.

https://doi.org/10.5194/egusphere-2025-4261
Preprint. Discussion started: 20 October 2025

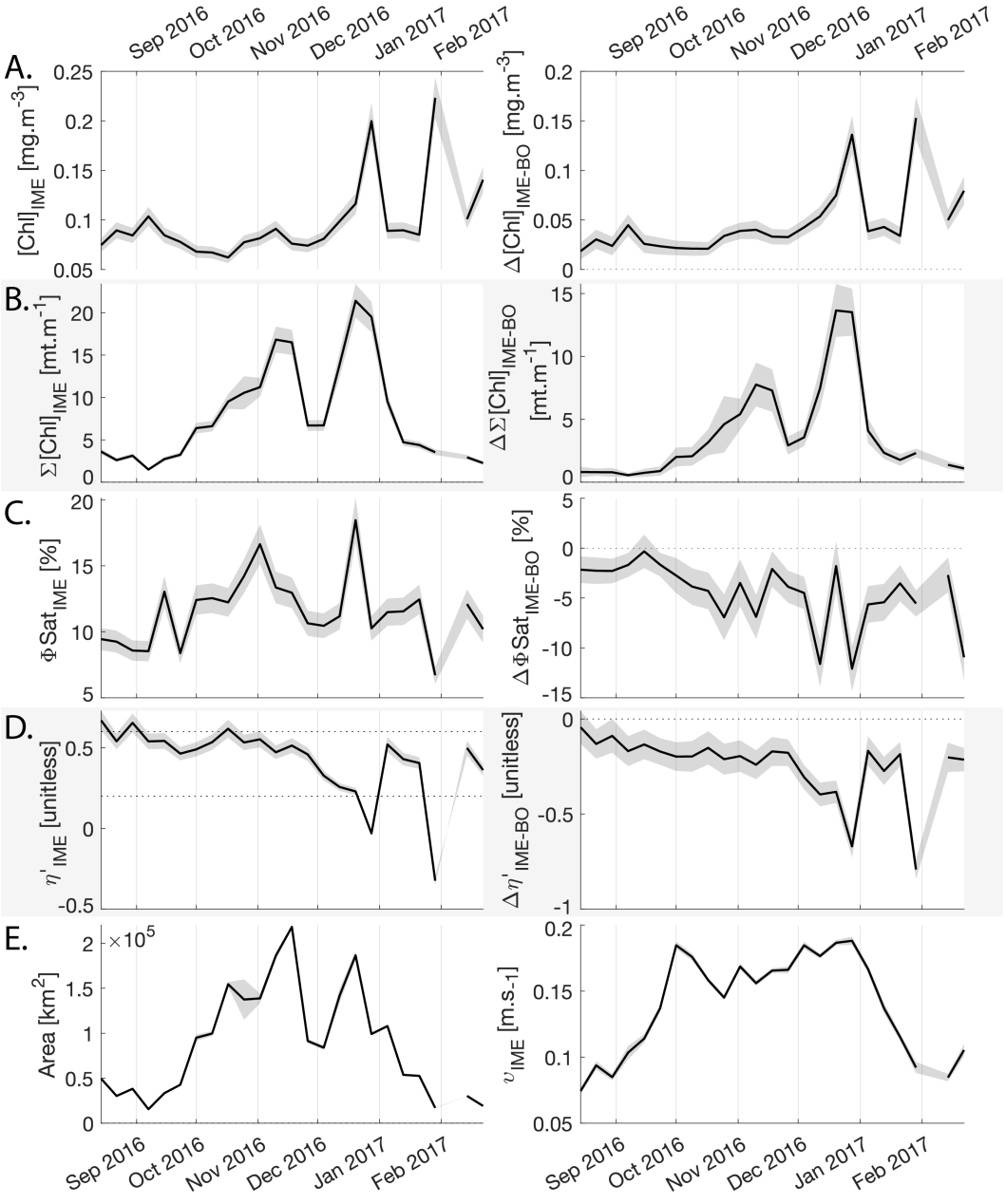

Figure E3. Six-month-long time series of satellite-derived IME properties of the IME zone detected around Samoa (Savaii, Upolu, and Tutuila). **A, B, C, and D left panels**: Average of properties within the IME zones, **A, B, C, and D right panels**: Difference between properties within the IME zones and the background ocean (BO). **A row**: chlorophyll *a* concentration ([Chla]), **B row**: IME integrated [Chla] ($\sum[Chla]_{IME}$), **C row**: fluorescence quantum yield (ϕ_{Sat}), **D row**: macronutrient stress index (η'), **E left:** IME zone area (in km^2), **E right**: surface current velocity.

https://doi.org/10.5194/egusphere-2025-4261
Preprint. Discussion started: 20 October 2025

References

Bailey, S. W. and Werdell, P. J.: A Multi-Sensor Approach for the on-Orbit Validation of Ocean Color Satellite Data Products, Remote Sensing of Environment, 102, 12–23, https://doi.org/10.1016/j.rse.2006.01.015, 2006.

Behrenfeld, M. J. and Boss, E.: Beam Attenuation and Chlorophyll Concentration as Alternative Optical Indices of Phytoplankton Biomass, Journal of Marine Research, 64, 431–451, 2006.

Behrenfeld, M. J. and Kolber, Z. S.: Widespread Iron Limitation of Phytoplankton in the South Pacific Ocean, Science, 283, 840–843, https://doi.org/10.1126/science.283.5403.840, 1999.

Behrenfeld, M. J. and Milligan, A. J.: Photophysiological Expressions of Iron Stress in Phytoplankton, Annual Review of Marine Science, 5, 217–246, https://doi.org/10.1146/annurev-marine-121211-172356, 2013.

Behrenfeld, M. J., Worthington, K., Sherrell, R. M., Chavez, F. P., Strutton, P., McPhaden, M., and Shea, D. M.: Controls on Tropical Pacific Ocean Productivity Revealed through Nutrient Stress Diagnostics, Nature, 442, 1025–1028, https://doi.org/10.1038/nature05083, 2006.

Behrenfeld, M. J., Westberry, T. K., Boss, E. S., O'Malley, R. T., Siegel, D. A., Wiggert, J. D., Franz, B. A., McClain, C. R., Feldman, G. C., Doney, S. C., Moore, J. K., Dall'Olmo, G., Milligan, A. J., Lima, I., and Mahowald, N.: Satellite-Detected Fluorescence Reveals Global Physiology of Ocean Phytoplankton, Biogeosciences, 6, 779–794, https://doi.org/10.5194/bg-6-779-2009, 2009.

Behrenfeld, M. J., O'Malley, R. T., Boss, E. S., Westberry, T. K., Graff, J. R., Halsey, K. H., Milligan, A. J., Siegel, D. A., and Brown, M. B.: Revaluating Ocean Warming Impacts on Global Phytoplankton, Nature Climate Change, 6, 323–330, https://doi.org/10.1038/nclimate2838, 2015.

Berman-Frank, I., Cullen, J. T., Shaked, Y., Sherrell, R. M., and Falkowski, P. G.: Iron Availability, Cellular Iron Quotas, and Nitrogen Fixation in *Trichodesmium*, Limnology and Oceanography, 46, 1249–1260, https://doi.org/10.4319/lo.2001.46.6.1249, 2001a.

Berman-Frank, I., Lundgren, P., Chen, Y.-B., Küpper, H., Kolber, Z., Bergman, B., and Falkowski, P.: Segregation of Nitrogen Fixation and Oxygenic Photosynthesis in the Marine Cyanobacterium *Trichodesmium*, Science, 294, 1534–1537, https://doi.org/10.1126/science.1064082, 2001b.

Bishop, J. K. B., Calvert, S. E., and Soon, M. Y.: Spatial and Temporal Variability of POC in the Northeast Subarctic Pacific, Deep Sea Research Part II: Topical Studies in Oceanography, 46, 2699–2733, https://doi.org/10.1016/S0967-0645(99)00081-8, 1999.

Bisson, K. M., Boss, E., Werdell, P. J., Ibrahim, A., and Behrenfeld, M. J.: Particulate Backscattering in the Global Ocean: A Comparison of Independent Assessments, Geophysical Research Letters, 48, e2020GL090 909, https://doi.org/10.1029/2020GL090909, 2021.

Bonnet, S., Guieu, C., Taillandier, V., Boulart, C., Bouruet-Aubertot, P., Gazeau, F., Scalabrin, C., Bressac, M., Knapp, A. N., Cuypers, Y., González-Santana, D., Forrer, H. J., Grisoni, J.-M., Grosso, O., Habasque, J., Jardin-Camps, M., Leblond, N., Le Moigne, F. A. C., Lebourges-Dhaussy, A., Lory, C., Nunige, S., Pulido-Villena, E., Rizzo, A. L., Sarthou, G., and Tilliette, C.: Natural Iron Fertilization by Shallow Hydrothermal Sources Fuels Diazotroph Blooms in the Ocean, Science, 380, 812–817, https://doi.org/10.1126/science.abq4654, 2023.

Boss, E., Twardowski, M. S., and Herring, S.: Shape of the Particulate Beam Attenuation Spectrum and Its Inversion to Obtain the Shape of the Particulate Size Distribution, Applied Optics, 40, 4885, https://doi.org/10.1364/AO.40.004885, 2001.

Boss, E., Picheral, M., Leeuw, T., Chase, A., Karsenti, E., Gorsky, G., Taylor, L., Slade, W., Ras, J., and Claustre, H.: The Characteristics of Particulate Absorption, Scattering and Attenuation Coefficients in the Surface Ocean; Contribution of the Tara Oceans Expedition, Methods in Oceanography, 7, 52–62, https://doi.org/10.1016/j.mio.2013.11.002, 2013.

https://doi.org/10.5194/egusphere-2025-4261
Preprint. Discussion started: 20 October 2025

Boss, E., Haëntjens, N., Ackleson, S. G., Balch, B., Chase, A., Dall'Olmo, G., Freeman, S., Liu, Y., Loftin, J., Neary, W., Nelson, N., Novak, M., Slade, W. H., Proctor, C. W., Tortell, P., and Westberry, T. K.: Ocean Optics & Biogeochemistry Protocols for Satellite Ocean Colour Sensor Validation. Volume 4: Inherent Optical Property Measurements and Protocols: Best Practices for the Collection and Processing of Ship-Based Underway Flow-Through Optical Data (V. 4.0)., IOCCG Protocol Series, 4, 1–22, https://doi.org/10.25607/OBP-664, 2019.

Bourdin, G.: Dynamics of Island Mass Effect: Multi-Satellite Binning Package, Zenodo [code], https://doi.org/10.5281/ZENODO.13376825, 2024.

Bourdin, G.: Dynamics of Island Mass Effect: Detection Input & Output Data, Zenodo [data set & code], https://doi.org/10.5281/ZENODO.14927568, 2025.

Bourdin, G. and Boss, E.: Continuous Underway Data Recorded during the Tara Pacific Expedition, https://doi.org/10.5067/SEABASS/TARA_PACIFIC_EXPEDITION/DATA001, 2016.

Bourdin, G. and Karp-Boss, L.: Pigment Concentrations Derived from High-Performance Liquid Chromatography (HPLC) Analysis from Samples Collected during the Tara Pacific Expedition from 2016-2018, Biological and Chemical Oceanography Data Management Office (BCO-DMO) [data set], https://doi.org/10.26008/1912/BCO-DMO.889930.1, 2023.

Bourdin, G., Karp-Boss, L., Lombard, F., Gorsky, G., and Boss, E.: Dynamics of the Island Mass Effect – Part 1: Detecting the Extent, Biogeosciences, 22, 3207–3233, https://doi.org/10.5194/bg-22-3207-2025, 2025.

Caferri, R., Guardini, Z., Bassi, R., and Dall'Osto, L.: Assessing Photoprotective Functions of Carotenoids in Photosynthetic Systems of Plants and Green Algae, in: Methods in Enzymology, vol. 674, pp. 53–84, Elsevier, https://doi.org/10.1016/bs.mie.2022.04.006, 2022.

Caputi, L., Carradec, Q., Eveillard, D., Kirilovsky, A., Pelletier, E., Pierella Karlusich, J. J., Rocha Jimenez Vieira, F., Villar, E., Chaffron, S., Malviya, S., Scalco, E., Acinas, S. G., Alberti, A., Aury, J.-M., Benoiston, A.-S., Bertrand, A., Biard, T., Bittner, L., Boccara, M., Brum, J. R., Brunet, C., Busseni, G., Carratalà, A., Claustre, H., Coelho, L. P., Colin, S., D'Aniello, S., Da Silva, C., Del Core, M., Doré, H., Gasparini, S., Kokoszka, F., Jamet, J.-L., Lejeusne, C., Lepoivre, C., Lescot, M., Lima-Mendez, G., Lombard, F., Lukeš, J., Maillet, N., Madoui, M.-A., Martinez, E., Mazzocchi, M. G., Néou, M. B., Paz-Yepes, J., Poulain, J., Ramondenc, S., Romagnan, J.-B., Roux, S., Salvagio Manta, D., Sanges, R., Speich, S., Sprovieri, M., Sunagawa, S., Taillandier, V., Tanaka, A., Tirichine, L., Trottier, C., Uitz, J., Veluchamy, A., Veselá, J., Vincent, F., Yau, S., Kandels-Lewis, S., Searson, S., Dimier, C., Picheral, M., Tara Oceans Coordinators, Bork, P., Boss, E., De Vargas, C., Follows, M. J., Grimsley, N., Guidi, L., Hingamp, P., Karsenti, E., Sordino, P., Stemmann, L., Sullivan, M. B., Tagliabue, A., Zingone, A., Garczarek, L., d'Ortenzio, F., Testor, P., Not, F., d'Alcalà, M. R., Wincker, P., Bowler, C., and Iudicone, D.: Community-Level Responses to Iron Availability in Open Ocean Plankton Ecosystems, Global Biogeochemical Cycles, 33, 391–419, https://doi.org/10.1029/2018GB006022, 2019.

Carder, K. L., Chen, F. R., and Hawes, S. K.: Instantaneous Photosynthetically Available Radiation and Absorbed Radiation by Phytoplankton, Tech. rep., College of Marine Science, University of South Florida, St. Petersburg, Florida 33701, 2003.

Chase, A., Boss, E., Zaneveld, R., Bricaud, A., Claustre, H., Ras, J., Dall'Olmo, G., and Westberry, T. K.: Decomposition of in Situ Particulate Absorption Spectra, Methods in Oceanography, 7, 110–124, https://doi.org/10.1016/j.mio.2014.02.002, 2013.

Connell, P., Ribalet, F., Armbrust, E., White, A., and Caron, D.: Diel Oscillations in the Feeding Activity of Heterotrophic and Mixotrophic Nanoplankton in the North Pacific Subtropical Gyre, Aquatic Microbial Ecology, 85, 167–181, https://doi.org/10.3354/ame01950, 2020.

Consortium, T. P.: Tara Pacific Expedition Participants, Zenodo, https://doi.org/10.5281/ZENODO.3777760, 2020.

Dall'Olmo, G., Westberry, T. K., Behrenfeld, M. J., Boss, E., and Slade, W. H.: Significant Contribution of Large Particles to Optical Backscattering in the Open Ocean, Biogeosciences, 6, 947–967, https://doi.org/10.5194/bg-6-947-2009, 2009.

https://doi.org/10.5194/egusphere-2025-4261
Preprint. Discussion started: 20 October 2025

Dandonneau, Y. and Charpy, L.: An Empirical Approach to the Island Mass Effect in the South Tropical Pacific Based on Sea Surface Chlorophyll Concentrations, Deep-Sea Res. Pt. I, 32, 707–721, https://doi.org/10.1016/0198-0149(85)90074-3, 1985.

De Falco, C., Desbiolles, F., Bracco, A., and Pasquero, C.: Island Mass Effect: A Review of Oceanic Physical Processes, Frontiers in Marine Science, 9, 894 860, https://doi.org/10.3389/fmars.2022.894860, 2022.

European Union-Copernicus Marine Service: Global Ocean Ensemble Physics Reanalysis, Mercator Ocean International [data set], https://doi.org/10.48670/MOI-00024, 2019.

Falkowski, P. G. and Owens, T. G.: Light—Shade Adaptation: Two Strategies in Marine Phytoplankton., Plant Physiology, 66, 592–595, https://doi.org/10.1104/pp.66.4.592, 1980.

Frouin, R. and Pinker, R. T.: Estimating Photosynthetically Active Radiation (PAR) at the Earth's Surface from Satellite Observations, Remote Sensing of Environment, 51, 98–107, https://doi.org/10.1016/0034-4257(94)00068-X, 1995.

Gardner, W., Mishonov, A., and Richardson, M.: Global POC Concentrations from In-Situ and Satellite Data, Deep Sea Research Part II: Topical Studies in Oceanography, 53, 718–740, https://doi.org/10.1016/j.dsr2.2006.01.029, 2006.

Gardner, W. D., Richardson, M. J., Carlson, C. A., Hansell, D., and Mishonov, A. V.: Determining True Particulate Organic Carbon: Bottles, Pumps and Methodologies, Deep Sea Research Part II: Topical Studies in Oceanography, 50, 655–674, https://doi.org/10.1016/S0967-0645(02)00589-1, 2003.

GEBCO Bathymetric Compilation Group: The GEBCO_2022 Grid - a Continuous Terrain Model of the Global Oceans and Land., NERC EDS British Oceanographic Data Centre NOC [data set], https://doi.org/10.5285/E0F0BB80-AB44-2739-E053-6C86ABC0289C, 2022.

Geider, R. J., Maclntyre, H. L., and Kana, T. M.: A Dynamic Regulatory Model of Phytoplanktonic Acclimation to Light, Nutrients, and Temperature, Limnology and Oceanography, 43, 679–694, https://doi.org/10.4319/lo.1998.43.4.0679, 1998.

Goes, J., Saino, T., Oaku, H., and Jiang, D.: A Method for Estimating Sea Surface Nitrate Concentrations from Remotely Sensed SST and Chlorophyll A-a Case Study for the North Pacific Ocean Using OCTS/ADEOS Data, IEEE Transactions on Geoscience and Remote Sensing, 37, 1633–1644, https://doi.org/10.1109/36.763279, 1999.

Gorsky, G., Bourdin, G., Lombard, F., Pedrotti, M. L., Audrain, S., Bin, N., Boss, E., Bowler, C., Cassar, N., Caudan, L., Chabot, G., Cohen, N. R., Cron, D., De Vargas, C., Dolan, J. R., Douville, E., Elineau, A., Flores, J. M., Ghiglione, J. F., Haëntjens, N., Hertau, M., John, S. G., Kelly, R. L., Koren, I., Lin, Y., Marie, D., Moulin, C., Moucherie, Y., Pesant, S., Picheral, M., Poulain, J., Pujo-Pay, M., Reverdin, G., Romac, S., Sullivan, M. B., Trainic, M., Tressol, M., Troublé, R., Vardi, A., Voolstra, C. R., Wincker, P., Agostini, S., Banaigs, B., Boissin, E., Forcioli, D., Furla, P., Galand, P. E., Gilson, E., Reynaud, S., Sunagawa, S., Thomas, O. P., Thurber, R. L. V., Zoccola, D., Planes, S., Allemand, D., and Karsenti, E.: Expanding Tara Oceans Protocols for Underway, Ecosystemic Sampling of the Ocean-Atmosphere Interface During Tara Pacific Expedition (2016–2018), Frontiers in Marine Science, 6, 750, https://doi.org/10.3389/fmars.2019.00750, 2019.

Gove, J. M., McManus, M. A., Neuheimer, A. B., Polovina, J. J., Drazen, J. C., Smith, C. R., Merrifield, M. A., Friedlander, A. M., Ehses, J. S., Young, C. W., Dillon, A. K., and Williams, G. J.: Near-Island Biological Hotspots in Barren Ocean Basins, Nature Communications, 7, 10 581, https://doi.org/10.1038/ncomms10581, 2016.

Graff, J. R., Westberry, T. K., Milligan, A. J., Brown, M. B., Dall'Olmo, G., van Dongen-Vogels, V., Reifel, K. M., and Behrenfeld, M. J.: Analytical Phytoplankton Carbon Measurements Spanning Diverse Ecosystems, Deep Sea Research Part I: Oceanographic Research Papers, 102, 16–25, https://doi.org/10.1016/j.dsr.2015.04.006, 2015.

https://doi.org/10.5194/egusphere-2025-4261
Preprint. Discussion started: 20 October 2025

Greene, R. M., Kolber, Z. S., Swift, D. G., Tindale, N. W., and Falkowski, P. G.: Physiological Limitation of Phytoplankton Photosynthesis in the Eastern Equatorial Pacific Determined from Variability in the Quantum Yield of Fluorescence, Limnology and Oceanography, 39, 1061–1074, https://doi.org/10.4319/lo.1994.39.5.1061, 1994.

Guieu, C., Bonnet, S., Petrenko, A., Menkes, C., Chavagnac, V., Desboeufs, K., Maes, C., and Moutin, T.: Iron from a Submarine Source Impacts the Productive Layer of the Western Tropical South Pacific (WTSP), Scientific Reports, 8, 9075, https://doi.org/10.1038/s41598-018-27407-z, 2018.

Halsey, K. H. and Jones, B. M.: Phytoplankton Strategies for Photosynthetic Energy Allocation, Annual Review of Marine Science, 7, 265–297, https://doi.org/10.1146/annurev-marine-010814-015813, 2015.

Heywood, K. J., Barton, E. D., and Simpson, J. H.: The Effects of Flow Disturbance by an Oceanic Island, Journal of Marine Research, 48, 55–73, https://doi.org/10.1357/002224090784984623, 1990.

Hu, C., Feng, L., Lee, Z., Franz, B. A., Bailey, S. W., Werdell, P. J., and Proctor, C. W.: Improving Satellite Global Chlorophyll *a* Data Products Through Algorithm Refinement and Data Recovery, Journal of Geophysical Research: Oceans, 124, 1524–1543, https://doi.org/10.1029/2019JC014941, 2019.

Huot, Y., Antoine, D., and Vellucci, V.: Daily Sun-induced Chlorophyll Fluorescence vs. Irradiance Curves Reflect the Photoadaptation of Phytoplankton in Surface Waters, Limnology and Oceanography, p. lno.70001, https://doi.org/10.1002/lno.70001, 2025.

James, A. K., Washburn, L., Gotschalk, C., Maritorena, S., Alldredge, A., Nelson, C. E., Hench, J. L., Leichter, J. J., Wyatt, A. S. J., and Carlson, C. A.: An Island Mass Effect Resolved Near Mo'orea, French Polynesia, Frontiers in Marine Science, 7, 16, https://doi.org/10.3389/fmars.2020.00016, 2020.

Kolber, Z. S., Barber, R. T., Coale, K. H., Fitzwateri, S. E., Greene, R. M., Johnson, K. S., Lindley, S., and Falkowski, P. G.: Iron Limitation of Phytoplankton Photosynthesis in the Equatorial Pacific Ocean, Nature, 371, 145–149, https://doi.org/10.1038/371145a0, 1994.

Kramer, S. J. and Siegel, D. A.: How Can Phytoplankton Pigments Be Best Used to Characterize Surface Ocean Phytoplankton Groups for Ocean Color Remote Sensing Algorithms?, Journal of Geophysical Research: Oceans, 124, 7557–7574, https://doi.org/10.1029/2019JC015604, 2019.

Küpper, H., Šetlík, I., Seibert, S., Prášil, O., Šetlikova, E., Strittmatter, M., Levitan, O., Lohscheider, J., Adamska, I., and Berman-Frank, I.: Iron Limitation in the Marine Cyanobacterium *Trichodesmium* Reveals New Insights into Regulation of Photosynthesis and Nitrogen Fixation, New Phytologist, 179, 784–798, https://doi.org/10.1111/j.1469-8137.2008.02497.x, 2008.

Laws, E. A. and Bannister, T. T.: Nutrient- and Light-limited Growth of Thalassiosira Fluviatilis in Continuous Culture, with Implications for Phytoplankton Growth in the Ocean1, Limnology and Oceanography, 25, 457–473, https://doi.org/10.4319/lo.1980.25.3.0457, 1980.

Lee, Z., Carder, K. L., and Arnone, R. A.: Deriving Inherent Optical Properties from Water Color: A Multiband Quasi-Analytical Algorithm for Optically Deep Waters, Applied Optics, 41, 5755, https://doi.org/10.1364/AO.41.005755, 2002.

Lee, Z., Lubac, B., Werdell, J., and Arnone, R.: An Update of the Quasi-Analytical Algorithm (QAA_v5), International Ocean Color Group Software Report, pp. 1–9, 2009.

Lee, Z., Hu, C., Shang, S., Du, K., Lewis, M., Arnone, R., and Brewin, R.: Penetration of UV-visible Solar Radiation in the Global Oceans: Insights from Ocean Color Remote Sensing., Journal of Geophysical Research: Oceans, 118, 4241–4255, https://doi.org/10.1002/jgrc.20308, 2013.

Lehahn, Y., Koren, I., Sharoni, S., d'Ovidio, F., Vardi, A., and Boss, E.: Dispersion/Dilution Enhances Phytoplankton Blooms in Low-Nutrient Waters, Nature Communications, 8, 14 868, https://doi.org/10.1038/ncomms14868, 2017.

https://doi.org/10.5194/egusphere-2025-4261
Preprint. Discussion started: 20 October 2025

Litchman, E., Klausmeier, C. A., Schofield, O. M., and Falkowski, P. G.: The Role of Functional Traits and Trade-offs in Structuring Phytoplankton Communities: Scaling from Cellular to Ecosystem Level, Ecology Letters, 10, 1170–1181, https://doi.org/10.1111/j.1461-0248.2007.01117.x, 2007.

Livanou, E., Lagaria, A., Santi, I., Mandalakis, M., Pavlidou, A., Lika, K., and Psarra, S.: Pigmented and Heterotrophic Nanoflagellates: Abundance and Grazing on Prokaryotic Picoplankton in the Ultra-Oligotrophic Eastern Mediterranean Sea, Deep Sea Research Part II: Topical Studies in Oceanography, 164, 100–111, https://doi.org/10.1016/j.dsr2.2019.04.007, 2019.

Lombard, F., Bourdin, G., Pesant, S., Agostini, S., Baudena, A., Boissin, E., Cassar, N., Clampitt, M., Conan, P., Da Silva, O., Dimier, C., Douville, E., Elineau, A., Fin, J., Flores, J. M., Ghiglione, J.-F., Hume, B. C. C., Jalabert, L., John, S. G., Kelly, R. L., Koren, I., Lin, Y., Marie, D., McMinds, R., Mériguet, Z., Metzl, N., Paz-García, D. A., Pedrotti, M. L., Poulain, J., Pujo-Pay, M., Ras, J., Reverdin, G., Romac, S., Rouan, A., Röttinger, E., Vardi, A., Voolstra, C. R., Moulin, C., Iwankow, G., Banaigs, B., Bowler, C., De Vargas, C., Forcioli, D., Furla, P., Galand, P. E., Gilson, E., Reynaud, S., Sunagawa, S., Sullivan, M. B., Thomas, O. P., Troublé, R., Thurber, R. V., Wincker, P., Zoccola, D., Allemand, D., Planes, S., Boss, E., and Gorsky, G.: Open Science Resources from the Tara Pacific Expedition across Coral Reef and Surface Ocean Ecosystems, Scientific Data, 10, 324, https://doi.org/10.1038/s41597-022-01757-w, 2023.

Longhurst, A.: Ecological Geography of the Sea, Elsevier, second edition edn., https://doi.org/10.1016/B978-0-12-455521-1.X5000-1, 2007.

Martinez, E., Rodier, M., Pagano, M., and Sauzède, R.: Plankton Spatial Variability within the Marquesas Archipelago, South Pacific, Journal of Marine Systems, 212, 103 432, https://doi.org/10.1016/j.jmarsys.2020.103432, 2020.

Mériguet, Z., Bourdin, G., Jalabert, L., Bun, O., Caray–Counil, L., Elineau, A., Gorsky, G., and Lombard, F.: Global Scale Surface Micro-Plankton Dataset Collected with Deck Net and Imaged with FlowCam during the Tara Pacific Expedition, https://doi.org/10.17882/102697, 2024a.

Mériguet, Z., Bourdin, G., Kristan, N., Jalabert, L., Bun, O., Picheral, M., Caray–Counil, L., Maury, J., Pedrotti, M.-L., Elineau, A., Paz-Garcia, D. A., Karp-Boss, L., Gorsky, G., Lombard, F., and the Tara Pacific Consortium Coordinators team: Quantitative Imaging Datasets of Micro to Mesoplankton Communities and Surface Microplastic across the Pacific Ocean from the Tara Pacific Expedition, https://doi.org/10.5194/essd-2024-507, 2024b.

Messié, M., Petrenko, A., Doglioli, A. M., Aldebert, C., Martinez, E., Koenig, G., Bonnet, S., and Moutin, T.: The Delayed Island Mass Effect: How Islands Can Remotely Trigger Blooms in the Oligotrophic Ocean, Geophysical Research Letters, 47, https://doi.org/10.1029/2019GL085282, 2020.

Messié, M., Petrenko, A., Doglioli, A. M., Martinez, E., and Alvain, S.: Basin-Scale Biogeochemical and Ecological Impacts of Islands in the Tropical Pacific Ocean, Nature Geoscience, 15, 469–474, https://doi.org/10.1038/s41561-022-00957-8, 2022.

Morel, A., Huot, Y., Gentili, B., Werdell, P. J., Hooker, S. B., and Franz, B. A.: Examining the Consistency of Products Derived from Various Ocean Color Sensors in Open Ocean (Case 1) Waters in the Perspective of a Multi-Sensor Approach, Remote Sensing of Environment, 111, 69–88, https://doi.org/10.1016/j.rse.2007.03.012, 2007.

Nunn, P. D., Kumar, L., Eliot, I., and McLean, R. F.: Classifying Pacific Islands, Geoscience Letters, 3, 7, https://doi.org/10.1186/s40562-016-0041-8, 2016.

Olson, R., Sosik, H., Chekalyuk, A., and Shalapyonok, A.: Effects of Iron Enrichment on Phytoplankton in the Southern Ocean during Late Summer: Active Fluorescence and Flow Cytometric Analyses, Deep Sea Research Part II: Topical Studies in Oceanography, 47, 3181–3200, https://doi.org/10.1016/S0967-0645(00)00064-3, 2000.

O'Reilly, J. E. and Werdell, P. J.: Chlorophyll Algorithms for Ocean Color Sensors - OC4, OC5 & OC6, Remote Sensing of Environment, 229, 32–47, https://doi.org/10.1016/j.rse.2019.04.021, 2019.

https://doi.org/10.5194/egusphere-2025-4261
Preprint. Discussion started: 20 October 2025

Palacios, D. M.: Factors Influencing the Island-mass Effect of the Galápagos Archipelago, Geophysical Research Letters, 29, https://doi.org/10.1029/2002GL016232, 2002.

Petit, F., Uitz, J., Schmechtig, C., Dimier, C., Ras, J., Poteau, A., Golbol, M., Vellucci, V., and Claustre, H.: Influence of the Phytoplankton Community Composition on the in Situ Fluorescence Signal: Implication for an Improved Estimation of the Chlorophyll-a Concentration from BioGeoChemical-Argo Profiling Floats, Frontiers in Marine Science, 9, 959 131, https://doi.org/10.3389/fmars.2022.959131, 2022.

POLYMER flags: HYGEOS - POLYMER README Section: 2.6 Flagging, GitHub [code], last access: 2024-08.

Raapoto, H., Martinez, E., Petrenko, A., Doglioli, A., Gorgues, T., Sauzède, R., Maamaatuaiahutapu, K., Maes, C., Menkes, C., and Lefèvre, J.: Role of Iron in the Marquesas Island Mass Effect, Journal of Geophysical Research: Oceans, 124, 7781–7796, https://doi.org/10.1029/2019JC015275, 2019.

Raimbault, P., Garcia, N., and Cerutti, F.: Distribution of Inorganic and Organic Nutrients in the South Pacific Ocean – Evidence for Long-Term Accumulation of Organic Matter in Nitrogen-Depleted Waters, Biogeosciences, 5, 281–298, https://doi.org/10.5194/bg-5-281-2008, 2008.

Roesler, C., Uitz, J., Claustre, H., Boss, E., Xing, X., Organelli, E., Briggs, N., Bricaud, A., Schmechtig, C., Poteau, A., D'Ortenzio, F., Ras, J., Drapeau, S., Haëntjens, N., and Barbieux, M.: Recommendations for Obtaining Unbiased Chlorophyll Estimates from in Situ Chlorophyll Fluorometers: A Global Analysis of WET Labs ECO Sensors, Limnology and Oceanography: Methods, 15, 572–585, https://doi.org/10.1002/lom3.10185, 2017.

Sayre, R., Noble, S., Hamann, S., Smith, R., Wright, D., Breyer, S., Butler, K., Van Graafeiland, K., Frye, C., Karagulle, D., Hopkins, D., Stephens, D., Kelly, K., Basher, Z., Burton, D., Cress, J., Atkins, K., Van Sistine, D. P., Friesen, B., Allee, R., Allen, T., Aniello, P., Asaad, I., Costello, M. J., Goodin, K., Harris, P., Kavanaugh, M., Lillis, H., Manca, E., Muller-Karger, F., Nyberg, B., Parsons, R., Saarinen, J., Steiner, J., and Reed, A.: A New 30 Meter Resolution Global Shoreline Vector and Associated Global Islands Database for the Development of Standardized Ecological Coastal Units, Journal of Operational Oceanography, 12, S47–S56, https://doi.org/10.1080/1755876X.2018.1529714, 2019.

Sayre, R., Martin, M. T., Cress, J. J., Holmes, N., McDermott-Long, O., Weatherdon, L., Spatz, D., VanGraafeiland, K., and Will, D.: The Geography of Islands, in: GIS for Science: Applying Mapping and Spatial Analysis, Volume 2, edited by Esri Press, pp. 4–21, Esri Press, http://pubs.er.usgs.gov/publication/70217711, 2020.

Shiozaki, T., Kodama, T., and Furuya, K.: Large-scale Impact of the Island Mass Effect through Nitrogen Fixation in the Western South Pacific Ocean, Geophysical Research Letters, 41, 2907–2913, https://doi.org/10.1002/2014GL059835, 2014.

Signorini, S. R., McClain, C. R., and Dandonneau, Y.: Mixing and Phytoplankton Bloom in the Wake of the Marquesas Islands, Geophysical Research Letters, 26, 3121–3124, https://doi.org/10.1029/1999GL010470, 1999.

Slade, W. H., Boss, E., Dall'Olmo, G., Langner, M. R., Loftin, J., Behrenfeld, M. J., Roesler, C., and Westberry, T. K.: Underway and Moored Methods for Improving Accuracy in Measurement of Spectral Particulate Absorption and Attenuation, Journal of Atmospheric and Oceanic Technology, 27, 1733–1746, https://doi.org/10.1175/2010JTECHO755.1, 2010.

Smith, S. R., Dupont, C. L., McCarthy, J. K., Broddrick, J. T., Oborník, M., Horák, A., Füssy, Z., Cihlář, J., Kleessen, S., Zheng, H., McCrow, J. P., Hixson, K. K., Araújo, W. L., Nunes-Nesi, A., Fernie, A., Nikoloski, Z., Palsson, B. O., and Allen, A. E.: Evolution and Regulation of Nitrogen Flux through Compartmentalized Metabolic Networks in a Marine Diatom, Nature Communications, 10, 4552, https://doi.org/10.1038/s41467-019-12407-y, 2019.

Steinmetz, F.: HYGEOS - POLYMER v4.17beta2, GitHub [code], last access: 2023-12-22.

https://doi.org/10.5194/egusphere-2025-4261
Preprint. Discussion started: 20 October 2025

Steinmetz, F., Deschamps, P.-Y., and Ramon, D.: Atmospheric Correction in Presence of Sun Glint: Application to MERIS, Optics Express, 19, 9783, https://doi.org/10.1364/OE.19.009783, 2011.

Thuillier, G., Hersé, M., Labs, D., Foujols, T., Peetermans, W., Gillotay, D., Simon, P. C., and Mandel, H.: The Solar Spectral Irradiance from 200 to 2400 Nm as Measured by the SOLSPEC Spectrometer from the ATLAS and EURECA Missions., Solar Physics, 214, 1–22, 2003.

Wang, X. J., Behrenfeld, M., Le Borgne, R., Murtugudde, R., and Boss, E.: Regulation of Phytoplankton Carbon to Chlorophyll Ratio by Light, Nutrients and Temperature in the Equatorial Pacific Ocean: A Basin-Scale Model, Biogeosciences, 6, 391–404, https://doi.org/10.5194/bg-6-391-2009, 2009.

Whiteman, C. and Allwine, K.: Extraterrestrial Solar Radiation on Inclined Surfaces, Environmental Software, 1, 164–169, https://doi.org/10.1016/0266-9838(86)90020-1, 1986.

Yun-Chi, L., An-Yi, T., and Kuo-Ping, C.: Trophic Coupling between Synechococcus and Pigmented Nanoflagellates in the Coastal Waters of Taiwan, Western Subtropical Pacific, Journal of Oceanography, 65, 781–789, https://doi.org/10.1007/s10872-009-0065-1, 2009.